

# Design and Control of a Tunable-Stiffness Pneumatic Legged Hopping Robot

Rongqian Chen

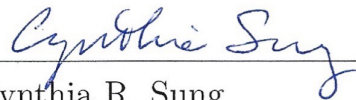
A THESIS

in

Electrical and System Engineering

Presented to the Faculties of the University of Pennsylvania in Partial  
Fulfillment of the Requirements for the Degree of Master of Science

2023



---

Cynthia R. Sung  
Gabel Family Term Assistant Professor  
Supervisor of Thesis



---

Tania Khanna  
Graduate Group Chair

# Acknowledgment

I would like to express my deepest gratitude to everyone who has played a vital role in the completion of this project. Your support, guidance, and encouragement have been invaluable throughout this journey.

First and foremost, I would like to thank my supervisor, Prof. Cynthia Sung, for her unwavering guidance, patience, and expertise. Her insights and constructive criticism have been instrumental in shaping this work, and I am truly grateful for her dedication and commitment.

I am also immensely grateful to the members helping me with this project. Thanks to Wei-Hsi Chen, for his valuable suggestions, critical feedback, and continuous support during the development of this project. My appreciation also goes to my colleague researcher, Jun Kwon, for his contributions, collaboration, and intellectual discussions that contributed to this project. Their diverse perspectives and expertise have enriched the quality of this work.

I would like to extend my gratitude to the members and staff at Sung Robotic Lab and Kodlab, for their assistance in providing the necessary resources and facilities for the successful completion of this project.

Lastly, I would like to acknowledge the financial support, without which this project would not have been possible.

To all those who have contributed to this journey, directly or indirectly, I extend my heartfelt appreciation and gratitude. Thank you for being a part of this milestone in my life.

# Abstract

Soft actuators show great potential in recent research due to their unique advantages compared to traditional actuators, such as flexibility, adaptability, versatility, and energy efficiency. This thesis presents the design, analysis, and evaluation of a monopedal hopper robot equipped with a novel pneumatic actuator capable of modulating stiffness during locomotion. The primary aim is to investigate the robot's energy efficiency and adaptability while traversing grounds with different stiffness. We conducted a series of experiments to evaluate the hopper robot's performance on different ground stiffness levels, enabling a comprehensive understanding of its energy consumption during the hopping process. Based on our findings, we propose several strategies to enhance the robot's locomotive efficiency and adaptability. These strategies provide insights into the development of energy-efficient legged robots, offering a foundation for further research and practical applications in various terrain exploration and navigation tasks.

# Contents

<b>1</b>	<b>Introduction</b>	<b>1</b>
1.1	Jumping Robot . . . . .	2
1.2	Soft Robots . . . . .	4
1.3	Problem Statement . . . . .	6
1.4	Contributions . . . . .	7
<b>2</b>	<b>Design Overview</b>	<b>9</b>
2.1	The Old vs New Hopper . . . . .	9
2.2	Mechanical Design . . . . .	13
2.2.1	Dual-bellow pneumatic actuator . . . . .	13
2.2.2	Molding Fabrication . . . . .	15
2.2.3	Anti-twisting regulator . . . . .	16
2.2.4	Motor and Pulley System . . . . .	18
2.2.5	Airtightness Enclosure . . . . .	19
2.3	Electronics . . . . .	20
2.4	Software . . . . .	23
2.5	Future Improvements . . . . .	26
<b>3</b>	<b>Bellows Model</b>	<b>27</b>
3.1	Model of Air Chamber and Spring System . . . . .	27
3.2	Bellow Stiffness Measurement and Analysis . . . . .	29

<b>4</b>	<b>Robot Model</b>	<b>33</b>
4.1	Hopper Leg Model . . . . .	33
4.2	Hopper Leg Simulation . . . . .	36
4.3	Hopper Dynamics Model . . . . .	38
4.4	Ground and Hopper Damping Measurement and Analysis . . . . .	41
4.4.1	Ground Stiffness Measurement . . . . .	42
4.4.2	Damping Measurement and Analysis . . . . .	43
4.5	Hopper Dynamics Simulation . . . . .	47
<b>5</b>	<b>Hopper Energy Efficiency Analysis</b>	<b>50</b>
5.1	Energy Cost of Altering Stiffness . . . . .	50
5.2	Hopping Height Equilibrium . . . . .	51
5.3	1D Hopping Energy Consumption . . . . .	55
<b>6</b>	<b>Conclusion</b>	<b>60</b>
6.1	Summary . . . . .	60
6.2	Future Work . . . . .	60
6.3	Lessons Learned . . . . .	61

# List of Tables

3.1	Bellow design overview . . . . .	30
3.2	Hopper stiffness MTS test result . . . . .	32
4.1	Ground stiffness MTS test result . . . . .	42
4.2	Hopper leg damping test data . . . . .	46
5.1	Parameters of equilibrium height simulation. . . . .	53
5.2	Parameters of equilibrium height experiment. . . . .	54
5.3	Parameters of damping energy loss simulation. . . . .	55
5.4	Hopper ground test data . . . . .	58

# List of Figures

1-1	Several jumper robots. (a) UCSB engineered jumper[7]. (b) Salto-1P.[8] (c) Locust-inspired jumping robot—TAUB[9]. (d)Mowgli[10]. (e) Pneumatic Robot[11]. (f) REBO hopper[3]. . . . .	4
1-2	Several soft controllable stiffness solutions. (a) EduBot with tunable stiffness C-legs[22]. (b)pneumatically actuated STIFF-FLOP manipulator[23]. (c) Granular jamming manipulator[24]. (d) SMA spring-driven InchBot[25]. (e) Elastomer with phase-changing metal alloy[26]. (f) Electro-Rheological fluids soft robot[27]. . . . .	6
2-1	(a) REBO Hopper. (b) Exploded view of Hopper design. (c) the crease pattern of REBO. The above images comes from [3], [29]. . . . .	10
2-2	(a) Hopper CAD view. (c) Physical hopper prototype. . . . .	12
2-3	Dual-bellow pneumatic actuators in the hopper. . . . .	14
2-4	(a) Bellow CAD parameters. (b) Mold core and cavity for bellow. (c) Physical bellow. . . . .	16
2-5	Experiment of bellow buckling. . . . .	17
2-6	(a) Bellow buckling. (b) Leg twisting. . . . .	17
2-7	Anti-twisting leg regulator. . . . .	18
2-8	(a) Pulley system CAD, with pulleys perspective view. (b) Physical pulley system. . . . .	19
2-9	Electronics on the hopper top plate. . . . .	20
2-10	Electronic system diagram . . . . .	21

2-11	Power management System Diagram . . . . .	22
2-12	State machine of controller. . . . .	24
2-13	Next version of hopper. . . . .	26
3-1	Air chamber and spring model . . . . .	28
3-2	Hopper leg stiffness test scenario. . . . .	31
3-3	(a) Simulation and experiment comparison. (b) stiffness changing with respect to air chamber displacement. . . . .	31
4-1	Hopper leg model . . . . .	34
4-2	Hopper leg model . . . . .	35
4-3	Convexity of energy function. . . . .	37
4-4	Bottom plate orientation and trajectory when tendon pulling for 30mm. Each figure corresponds to an initial actuator state: (a) [0 0 0], (b)[4 0 0], (c)[0 4 0], (d)[4 4 0], where each element in the 1x3 matrix pertains to a respective air-chamber compression in millimeters. . . . .	37
4-5	Hopper model . . . . .	38
4-6	Phases of hopping . . . . .	39
4-7	State machine of the model . . . . .	40
4-8	Toe-shape probe and ground material. . . . .	42
4-9	Ground damping test example. . . . .	45
4-10	Hopper leg damping test example. . . . .	45
4-11	Tests on the medium ground. (a) Hopping with soft leg. Actual and simulated pre-compression(mm): 37, 1.5. (b) Hopping with hard leg. Actual and simulated pre-compression(mm): 33, 0.8. . . . .	48
4-12	Figure 4-11: Tests on the soft ground. (a) Hopping with soft leg. Actual and simulated pre-compression(mm): 56, 1.5. (b) Hopping with hard leg. Actual and simulated pre-compression(mm): 53, 0.8. . . . .	49
5-1	Pololu motor energy consumption . . . . .	51

5-2	Simulation of Equilibrium Hopping Height. The left-hand side figures illustrate time-domain trajectories, while the right-hand side displays the phase portraits. Each pair of figures corresponds to a unique initial height from which the robot commences: (a,b) 200mm; (c,d) 170mm; (e,f) 150mm. . . . .	52
5-3	Trajectory of hopper body and foot in equilibrium height experiment.	54
5-4	Results of the damping energy loss simulation. (a) Damping loss when ground damping coefficient $d_g = 10$ , leg damping coefficient $d_l = 5$ . (b) Damping loss when ground damping coefficient $d_g = 2$ , leg damping coefficient $d_l = 5$ . . . . .	56
5-5	(a) Example data with unstable hops at the beginning. (b) Example data after the hopper approach the equilibrium state. . . . .	57

# Chapter 1

## Introduction

Legged robots have attracted significant attention in recent years due to their ability to navigate complex and uneven terrains, such as rocky surfaces, stairs, slopes, and even soft, unstable ground [1]. Their ability to adapt their leg positioning and foot contact points allows them to maintain stability and locomotion in environments that would be challenging for wheeled or tracked robots. On one hand, conventional terrestrial robotic locomotion methodologies appear to be confined to navigating obstacles that are of a comparative scale to their own dimensions. On the other hand, robots equipped with jumping capabilities could potentially overcome obstacles that are approximately an order of magnitude larger than their own size. This suggests a significant advantage and opens up new possibilities for robotic locomotion strategies in complex environments [2]. Their potential applications are in various fields such as search and rescue, exploration, and logistics.

In this thesis, the mechanical design, actuation system, hardware, software, and mathematical model of the hopper are demonstrated. The new design of a tunable-stiffness pneumatic actuator is able to actively perform a stiffness change during the actuation, without the assistance of bulky pumps and valves that are used by traditional pneumatic actuators. Compared to the previous hopping robot [3], the stiffness of our new actuation system is changeable. Several dynamic and kinematic models

are constructed to elucidate and forecast the behaviors of the hopper. Moreover, we built a physical prototype, and deploy a hierarchical high-speed real-time sensing and control system to tackle the challenge of high-speed locomotion.

## 1.1 Jumping Robot

Legged robots can be classified into different categories based on the number of legs, such as bipedal, quadrupedal, and hexapodal robots. Among the various types of legged robots, jumping robots represent a unique and intriguing subset that showcases the versatility of legged locomotion. Compared with walking and crawling behavior, jumping requires higher energy from robot actuators. This behavior allows the robot to transit through terrains more rapidly and interact with obstacles more efficiently. [4]. So some researchers are trying to utilize and imitate the biological functions of animals to design jumping robots.

Jumping robot research began decades ago, such as NASA's attempt to utilize the jumping robot embarked in Apollo series [5]. In recent years a large number of studies about bio-inspired jumping robots have been developed, and various actuators and energy storage mechanisms emerge [6], and several research are shown in Figure 1-1. Compared to other types of locomotion robots, the jumping robot's size plays a critical role in its overall performance [4]. Smaller robots have a distinct advantage in achieving higher energy-to-weight ratios, which can maximize either distance or height [2]. E.Hawkes [7] create an engineered device that can jump over 30 meters high, which transcends the physiological limitations of the biological jumper. It achieved high acceleration by multiplying the work done by the motor during the energy storage phase. By leveraging the lever arm and torsional spring mechanism, the robot can achieve a higher output energy than the input energy provided by the motor. Another example of increasing peak power for jumping and releasing more energy than muscle providing alone is [8], which presented a monopodal vertical jumping robot "Salto" that has high power-to-weight ratio, and can perform consecutive jumping

and direction change mid-air. Its agility attribute to its specialized tail and advanced control algorithms. Unlike the previous two, which use inverted pendulum structure, locust-inspired jumper TAUB [9] mimics locusts and use torsional spring for energy storage, the two torsion springs joining a pair of legs connected through a revolute joint driven by an electric motor. While those jumpers have the remarkable ability to achieve heights several times their own length, this performance is limited to a narrow range of sizes that can constrain the use of more complex mechanisms and their ability to tackle more sophisticated tasks, such as self-righting mechanisms and jumping speed, azimuth and elevation adjustment. The design trade-offs required to optimize for jumping performance can result in trade-offs in other aspects of the robot's performance. For instance, the employment of intricate mechanisms may necessitate a larger physical size; Augmenting energy storage capacities typically demands stronger structural components, which consequently contribute to the increased overall weight.

Moreover, in addition to smaller-sized jumpers, some relatively larger-scale jumper robots have been developed to enable more complex actuation systems and heavier load capacity. One such robot, Mowgli [10], features an artificial musculoskeletal system consisting of six McKibben pneumatic muscle actuators that can achieve jump heights exceeding 50% of its body height while maintaining a soft landing. Another pneumatic-actuated jumper [11] relies on energy stored in a cylinder that is replenished by a solenoid valve injecting high-pressure air during each jumping cycle. Alternatively, novel actuation strategies involving origami actuators [3], shape memory alloy springs [12], or dielectric elastomers [13] have been explored. These innovative approaches unlock new potential for actuation in robotics, paving the way for future investigations and advancements in the field.

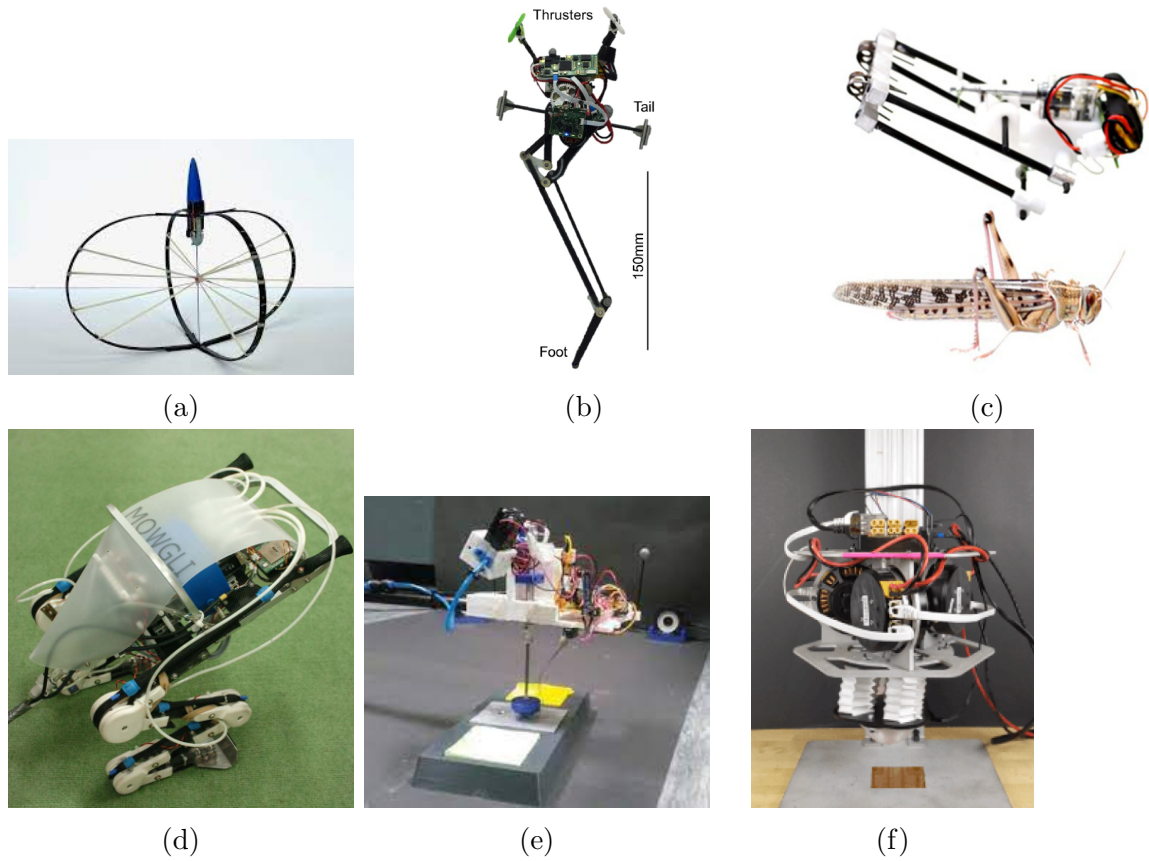


Figure 1-1: Several jumper robots. (a) UCSB engineered jumper[7]. (b) Salto-1P.[8] (c) Locust-inspired jumping robot—TAUB[9]. (d)Mowgli[10]. (e) Pneumatic Robot[11]. (f) REBO hopper[3].

## 1.2 Soft Robots

Both soft robotics and legged robotics often draw inspiration from biological systems. Many legged robots are designed to mimic the gait and mobility of animals by using rigid structures as their mechanism [1]. Compared to rigid robots, soft robots have tremendous potential and several advantages. It involves compliant materials with a structure inspired by biological systems, which gives them flexibility, and adaptability. Typically, a soft robot can be lightweight and dynamically adapt to changing environmental conditions, which is challenging for rigid robots [14]. Due to their unique features, soft robots have a considerable range of applications, including healthcare

treatments, wearable devices, and various tasks in extreme environments[15].

Similar to natural systems, soft robotic technologies facilitate the modulation of stiffness during actuation processes. This is exemplified in biological systems, such as muscles, where the stiffness varies between the passive (low stiffness) and active (high stiffness) states. Soft robots also employ comparable techniques to generate forces and modulate their load through stiffness modulation[16]. Recent advances in smart materials further exploit their softness for efficient movement by altering natural mechanical properties. The actuators composed of smart materials can change shape and stiffness in two ways[15, 17]: the first is based on the change of structure, such as mechanical solutions(Figure 1-2a), fluid-based solutions(Figure 1-2b), and jamming(Figure 1-2c). Another is changing the elastic properties, such as some materials are responsive to heat(Figure 1-2d, 1-2e) and electrical stimulation(Figure 1-2f). These solutions allow robots to perform a wide range of locomotion modes, including walking, crawling, rolling, jumping, and swimming[18].

One essential aspect of soft robotics is the ability to control and modulate the stiffness of the robot to match its environment[19]. In the context of legged robots, this matching of compliance enables the robot to interact more effectively, and efficiently with its surroundings, leading to improved performance[20, 21]. To achieve this, the robot’s control system must be able to adjust its compliance level to optimize its interaction with the environment or objects based on specific task requirements. Pneumatic actuators, which leverage pressurized gas to induce motion, are a potential solution due to their inherent compliance, rapid actuation, and high power density[18]. In this thesis, we present the development of a jumper robot with tunable stiffness pneumatic actuators that enable compliance matching during locomotion. The robot’s leg can adapt its stiffness to match the compliance of the ground, making the locomotion more energy-efficient and effective.

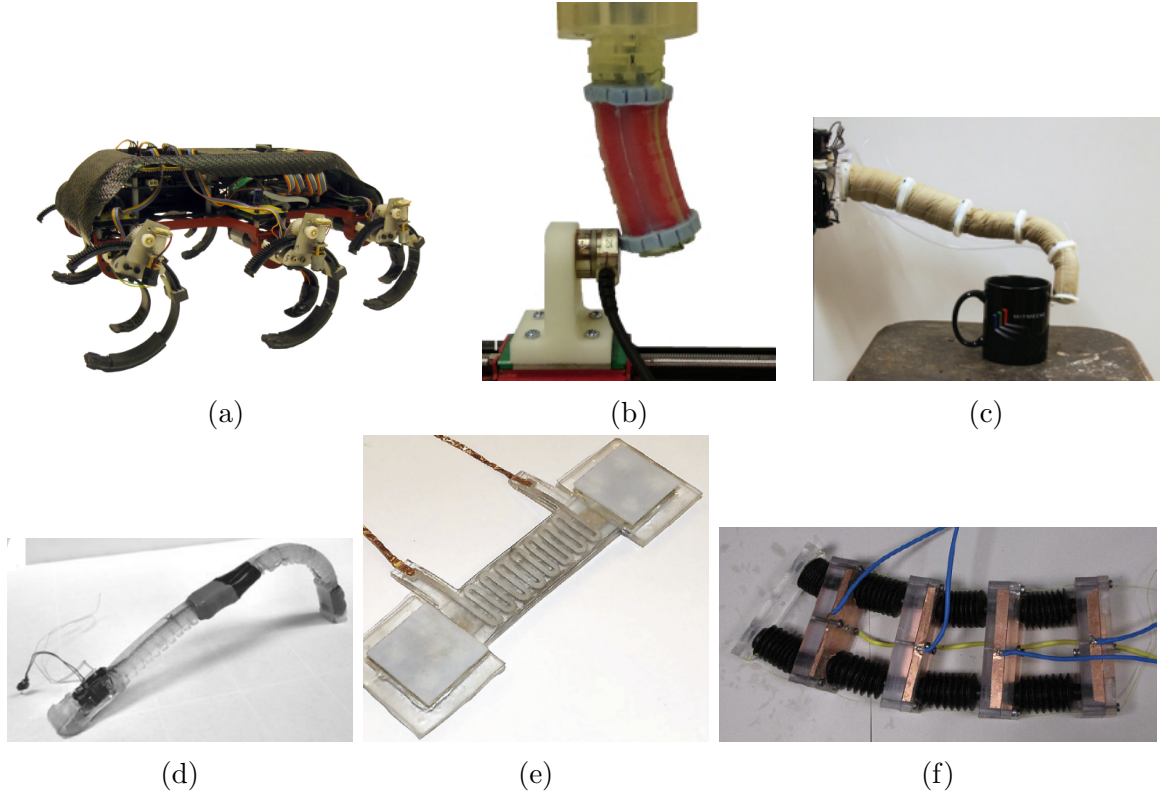


Figure 1-2: Several soft controllable stiffness solutions. (a) EduBot with tunable stiffness C-legs[22]. (b) pneumatically actuated STIFF-FLOP manipulator[23]. (c) Granular jamming manipulator[24]. (d) SMA spring-driven InchBot[25]. (e) Elastomer with phase-changing metal alloy[26]. (f) Electro-Rheological fluids soft robot[27].

### 1.3 Problem Statement

Energy efficiency and adaptability to varying ground conditions are critical challenges in the development of legged robots. Conventional legged robots often employ fixed-stiffness actuators, restricting their performance on uneven or changing terrain [22]. To address these challenges, it is essential to develop a changeable stiffness actuator capable of functioning in dynamic situations[22], offering a continuous and extensive stiffness range, precise control, and rapid response. However, achieving these goals remains difficult with current approaches.

Material-based solutions, such as shape-memory alloys (SMA) and low melting

point alloys, have demonstrated the ability to achieve a broad stiffness range [15]. However, these methods present challenges in controlling transition states and responsiveness, making them unsuitable for high-speed robots. Alternatively, mechanical-based approaches, such as jamming [28] and fluid-based solutions [27], offer greater controllability. Among these, pneumatic actuators provide a high work energy density and good linearity[18]. However, those pneumatic actuators requires bulky hardware such as external airsource which limits their applicability. Previous jumping robots utilizing pneumatic actuators, like McKibben pneumatic muscles [10] and pneumatic cylinders [11], which also require valves and air pumps to supply and regulate air pressure. Consequently, it is crucial to develop a lightweight pneumatic actuator that capitalizes on the advantages of pneumatic actuators while eliminating the need for bulky devices.

Aiming to solve the current legged robots’ issues such as high energy consumption and limited adaptability to diverse ground conditions, we propose the use of a variable stiffness pneumatic actuator to address these challenges, allowing the hopper robot to jump efficiently.

## 1.4 Contributions

This thesis presents the design and evaluation of a legged hopper robot equipped with a novel pneumatic actuator capable of varying stiffness and tested on grounds with different stiffness levels. Through 1D hopping experiments, we analyze its energy cost during the hopping process and assess its performance across various conditions. Our findings reveal a substantial improvement(up to 29.3% energy saving by changing leg stiffness, as shown in Table 5.4)and several strategies based on simulation results to further enhance the robot’s locomotive efficiency and adaptability.

The main contributions of this thesis are as follows:

- We proposed a novel dual-bellows structure for stiffness modulation, which elim-

inates the need for solenoid valves and air pumps, which significantly reduces the weight and energy cost. In addition, our bellows actuator permits a stiffness modification of approximately 1.42 times, as substantiated through experimental data detailed in Section 3.2.

- We developed mathematical models to describe and predict the stiffness change of the new pneumatic actuator, the leg segment behavior base on minimum total potential energy principle, and the dynamics of the hopper-ground interaction.
- We designed and built a hardware prototype of the hopper robot, including mechanical design, electronics, and software systems.
- Through experiments and analyses, we modeled the robot’s behavior, quantified the energy cost of the robot, and proposed energy-efficiency strategies for different ground conditions. These strategies provide valuable insights for future developments in legged robot locomotion and adaptability.

# Chapter 2

## Design Overview

### 2.1 The Old vs New Hopper

In previous work [3], a tendon-driven, parallel-spring, origami-based hopping machine was developed, utilizing a Reconfigurable Expanding Bistable Origami (REBO) pattern for efficient energy storage. The REBO bellows exhibit compliance in accordance with Hooke's law when compressed up to  $2/3$  of their length, demonstrating high durability and the ability to withstand thousands of loading and unloading cycles without physical damage. The lightweight and durable structure offers a broad range of stiffness, which can be adjusted by tuning the size and geometric parameters of the crease pattern, as shown in Figure 2-1(c).

The hopper is actuated by three DC motors, providing three degrees of freedom for each leg. Due to the absence of a self-righting mechanism, the hopper is mounted on a linear rail or fixed to a boom during vertical hopping tests. In the vertical hopping mode, the three REBO springs compress equally, while in the fore-aft hopping mode, the hopper imparts forward thrust by compressing the legs differently. The hopper operates in two modes, flight, and stance, using a strain resistance sensor to detect impacts and transition between modes. During the stance phase, the hopper sets its leg attitude and compression, and upon impact, releases the spring and lifts off.

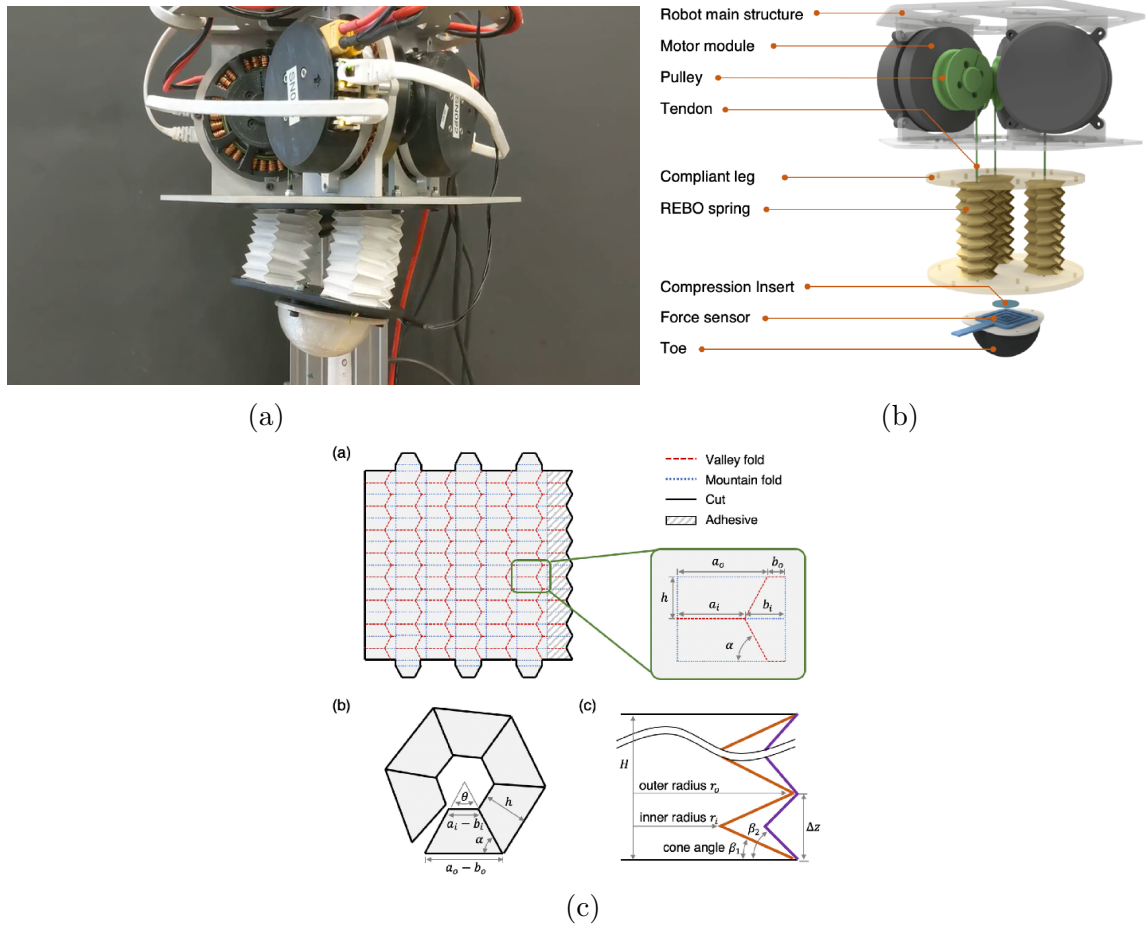


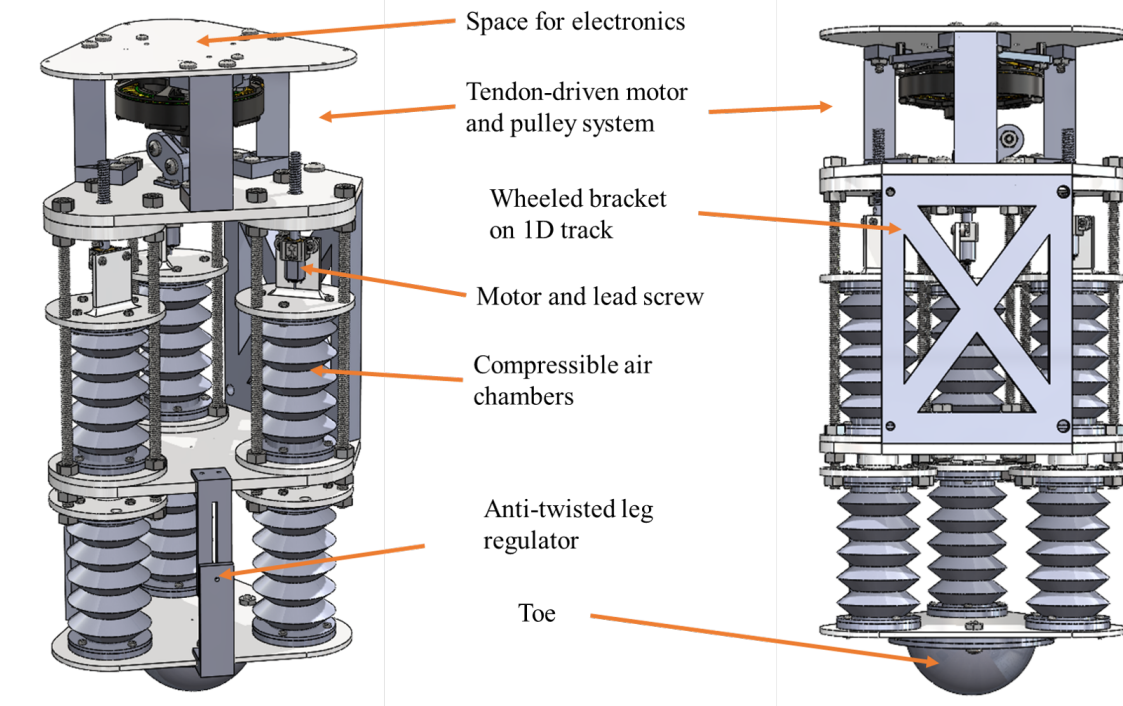
Figure 2-1: (a) REBO Hopper. (b) Exploded view of Hopper design. (c) the crease pattern of REBO. The above images comes from [3], [29].

In comparison to the preceding hopper model, the current design incorporates an Inertial Measurement Unit (IMU) for attitude sensing. This addition allows for the detection of not only impacts but also velocity, position, and orientation, thereby providing a comprehensive suite of motion data. The most significant alteration in the new design is the replacement of the fixed-stiffness REBO leg with a pneumatically actuated leg. These legs exhibit potential adaptability and require only a single U8 motor for tendon-driven actuation, thereby enhancing the overall efficiency of the hopper.

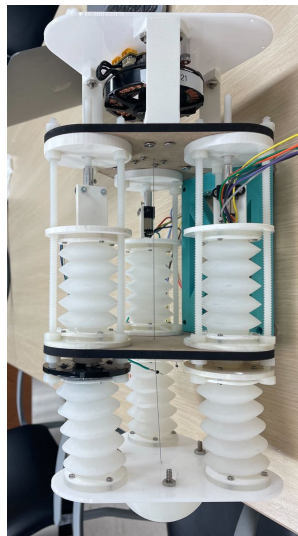
In our new hopper design, detailed shown in Figure 2-2, each actuator comprises

a pair of bellow-shaped air chambers and springs, both constructed from silicone and connected via threaded joints. The air chamber size is controlled by a motor and lead screw positioned above it; as the air chamber compresses, the pressurized air inside hardens the spring, as described in Section 3.1. The pneumatic actuators are actuated by a tendon running through the hole in the segment plates, passing through pulleys, and pulled by a horizontally placed brushless DC motor.

To modify leg orientation, the hopper compresses the air chambers to varying degrees, the stiffness change and elongation of the spring bellows can alter the leg posture, the math model is detailed present in Section 4.1.



(a)



(b)

Figure 2-2: (a) Hopper CAD view. (c) Physical hopper prototype.

## 2.2 Mechanical Design

1

In this section, we will delve into a comprehensive exposition of the mechanical structure along with the unique design decisions undertaken to address the significant challenges within the hopper. This detailed discussion aims to elucidate the mechanism by which the design elements aim to serve for better performance and solve these intricacies, hence contributing to the overall functionality of the hopper.

### 2.2.1 Dual-bellow pneumatic actuator

The bellows structure is a widely adopted mechanism in soft robotics, facilitating actuation through the expansion and contraction of a flexible, accordion-like structure. This structure typically comprises multiple interconnected compartments that can be pressurized to produce movement or force. By modulating the pressure in each compartment, the bellows structure can achieve various motions and deformations, rendering it a versatile and adaptable actuation mechanism. Among pneumatic actuators, a piston and cylinder can contract to a maximum of 50% of their extended length, while McKibben muscles can contract to approximately 70% of their extended length[30]. In contrast, the compression ratio of bellows is limited only by the thickness of the membrane bladder which connects bellow segments, allowing them to extend their length several times [30]. The structural advantage of bellows permits stiffness in compression while maintaining flexibility in bending. Additionally, bellows circumvent sliding friction and leakage issues that may complicate fluid-driven piston devices.

Owing to its simplicity and scalability, the bellows structure has been employed in various soft robotic applications, including grippers, manipulators [27], and locomotion systems [31]. The distinctive characteristics of this mechanism suggest it may be suitable for applications necessitating compliance, sensitivity, or adaptability,

---

<sup>1</sup>This work is done in collaboration with Jun Kwon.

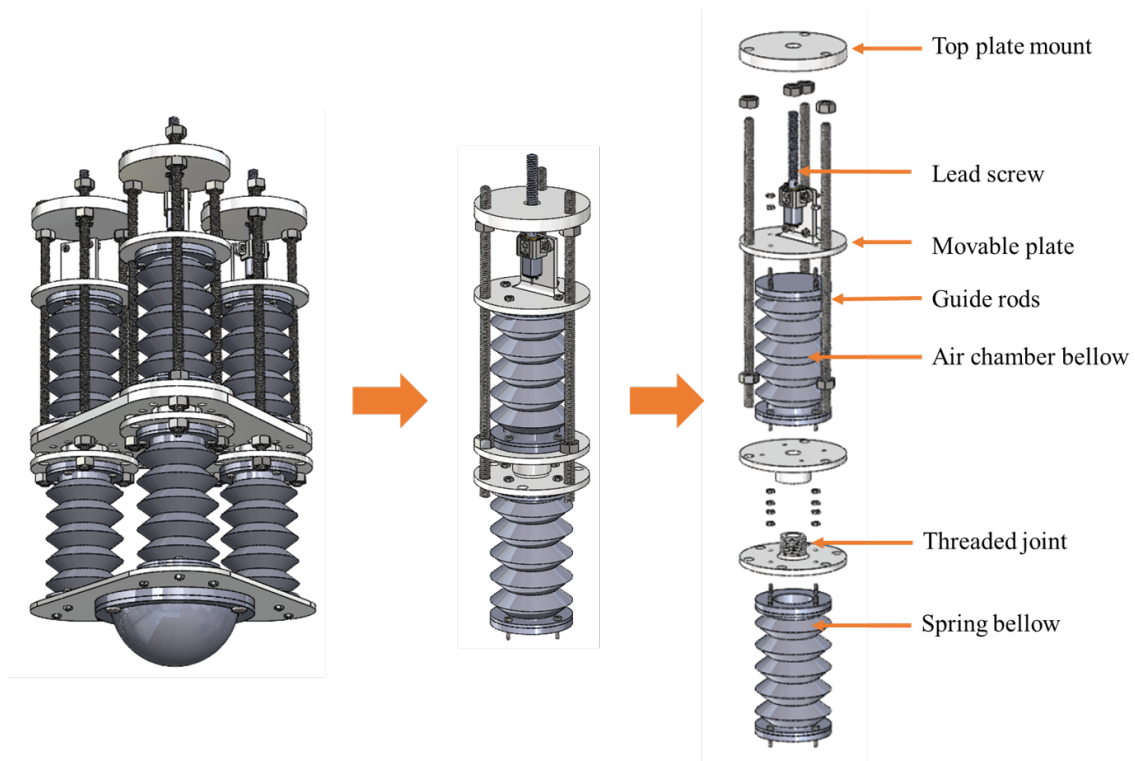


Figure 2-3: Dual-bellow pneumatic actuators in the hopper.

such as the task that is required to safely interact with humans or change their shape when interacting with dynamic environments.

In our hopper design, we incorporated three independent, enclosed dual-bellow actuators, as illustrated in Figure 2-3. For ease of disassembly, we utilized thread joints to connect each air chamber and spring, with a 10mm diameter hole inside. The hole size is critical to the actuator’s reaction time; during rapid hopping, air must flow freely between the two bellows to avoid lag and ensure the desired stiffness. The upper bellow functions as an air chamber, controlled by the motor and lead screw positioned above it. The plate to which the motor is mounted can move vertically along three guide rods. This movement is used to alter the volume within the actuator, thereby adjusting the air pressure and stiffness of the spring bellow located at the bottom. The three stiffness-varying springs allow the limb to achieve three DOF bending.[32].

## 2.2.2 Molding Fabrication

Various methods can be used to fabricate the bellows. Taking into account the laboratory equipment and complexity, we ultimately opted for two solutions: 3D printing and molding. For the 3D-printed components, we attempted to create a TPU spring, but it failed due to poor airtightness. We also experimented with SLA and flexible liquid filament for printing, but these materials were not strong enough and were prone to cracking.

In this research, we utilized the molding technique to construct bellow actuators that are strong, durable, flexible, and smooth-surfaced. To obtain an approximate estimate of the necessary bellow stiffness, the potential energy of the spring can be calculated using the formula:

$$\frac{1}{2}k\Delta x^2 = mgh \quad (2.1)$$

Assuming a robotic weight ( $m$ ) of 1.5 kg, and a desired hopping height ( $h$ ) of 20 mm achieved by a spring compression ( $\Delta x$ ) of 20 mm, the calculated spring stiffness would need to be 3000 N/m. Consequently, each spring would require a stiffness of approximately 1000 N/m.

After estimating the hardness required for the leg, we selected silicone rubber (Smooth-on MoldStar 31T) as the bellow material, which has a relatively high shore hardness of 30A. Due to the complex cavity shape inside the bellow, constructing it through one-time molding was challenging. As a result, we first divided the core and cavity into two parts, cast two half bellows separately, and then bonded them with silicone, as depicted in Figure 2-4.

The bellow has a wall thickness of 3mm, a segment height of 12.96mm, an inner radius of 10.58mm, and an outer radius of 20.10mm, as shown in Figure 2-4a. We selected these specific parameters not solely based on the stiffness range but also on the stability observed in practical tests. These tests indicated that bellows with more layers, a larger difference between inner and outer radius, and taller segments would

be more unstable. Thus, considering the trade-offs between high performance and stability, we opted for the current parameters of the bellow.

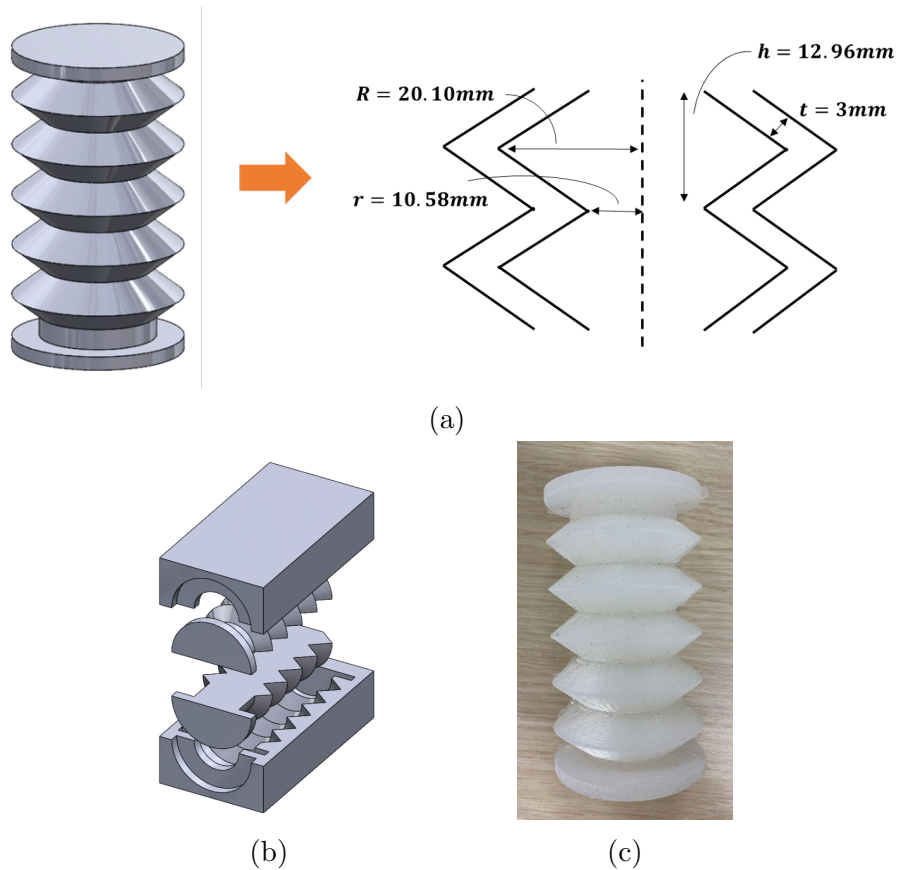


Figure 2-4: (a) Bellow CAD parameters. (b) Mold core and cavity for bellow. (c) Physical bellow.

### 2.2.3 Anti-twisting regulator

The phenomenon of buckling can occur in the bellow when the internal air pressure reaches a high level and exceeds the material's capacity to contain it, as depicted in Figure 2-6a. This abnormal deformation arises because the energy required for such a transformation is less than the energy necessary for deformation along the y-axis, leading to a shift in the actuator's stiffness. This buckling issue is visually demonstrated in Figure 2-5. The experimental setup comprises a syringe-bellow system that is sealed from the atmosphere, where the syringe is used to change the system

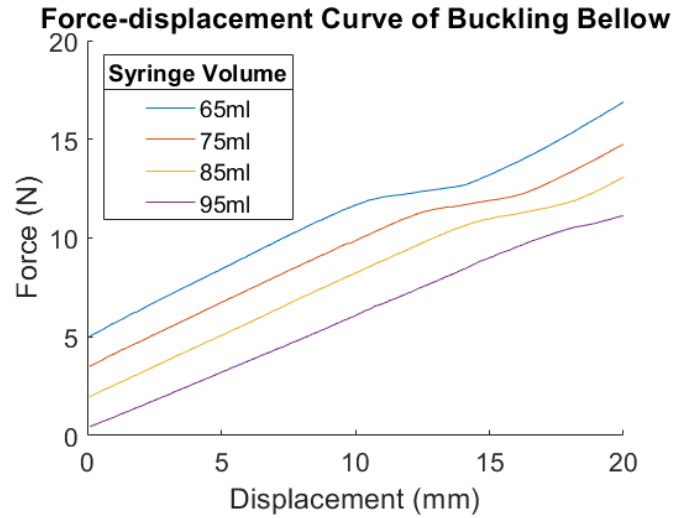


Figure 2-5: Experiment of bellow buckling.

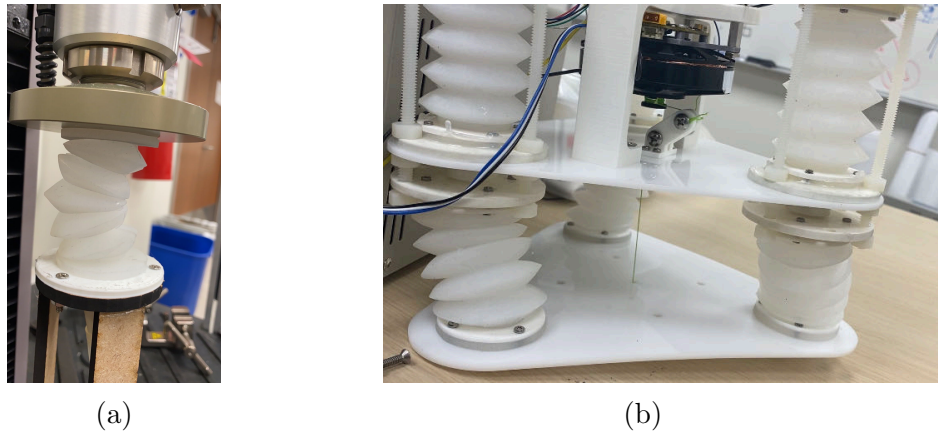


Figure 2-6: (a) Bellow buckling. (b) Leg twisting.

volume and bellow is under the MTS test plate. The syringe initiates at 95mm and is compressed to 65mm, while the probe of the MTS machine compresses from an equivalent height each time, thereby constraining the bellow's elongation. As per the plot, buckling happens when the curve's slope undergoes a significant alteration. Moreover, the buckling point reduces as the air pressure escalates, suggesting that heightened pressure might be the primary factor of buckling.

When buckling takes place, the bellow adopts a twisted shape, causing the robot's foot to twist. Consequently, a mechanical device is necessary to address this issue.

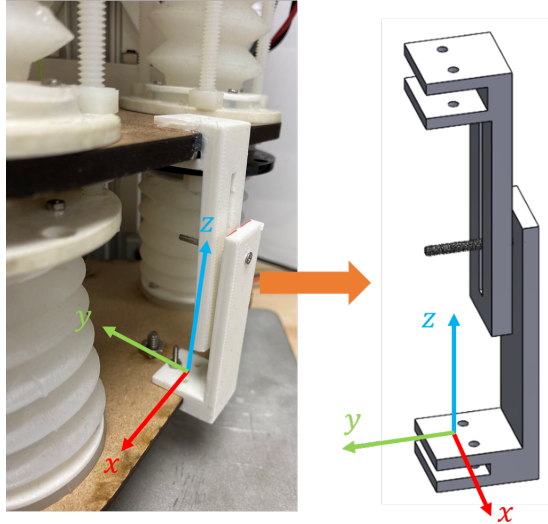


Figure 2-7: Anti-twisting leg regulator.

To tackle this problem, we designed an anti-twisting leg regulator to prevent buckling-induced twisting. This regulator permits relative motion between two parts along the z-direction or rotation around the x-axis while preventing rotation around the y-axis. In our experiments, the incorporation of two regulators effectively restricts leg-twisting motions, demonstrating the effectiveness of this approach.

#### 2.2.4 Motor and Pulley System

The hopper’s functionality is enabled by a tendon, manipulated by brushless DC motor(T-motor U8 KV100). Contrary to the previous design where motor shafts were oriented vertically to the ground for direct tendon pull, the current design incorporates a single tendon-driven motor. If the shaft were to be placed vertically in this design, the motor would be positioned on the side of the plate. This off-center placement of a heavy motor could result in shifting the center of mass which would disrupt the robot’s balance. To maintain symmetry, the motor is strategically located at the center of the plate, with pulleys utilized for guiding the tendon.

Nonetheless, the incorporation of a pulley system introduces friction-related challenges. Throughout the tightening and loosening cycles, the tendon’s interaction with

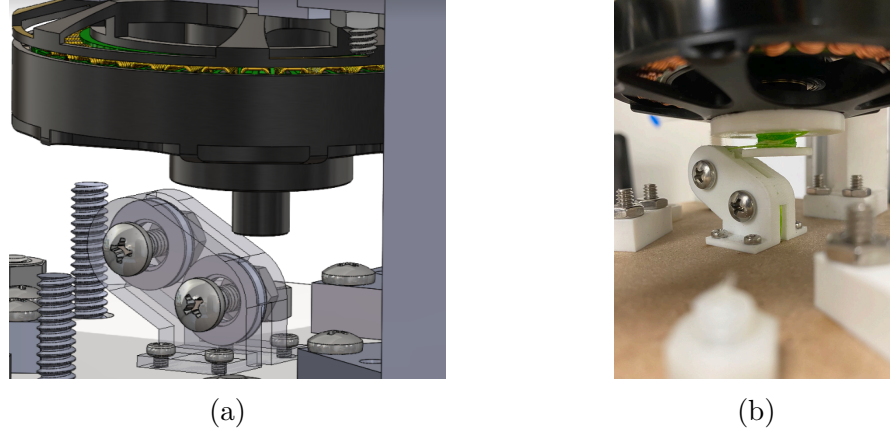


Figure 2-8: (a) Pulley system CAD, with pulleys perspective view. (b) Physical pulley system.

the pulley raises the risk of disengagement, potentially damaging the motor or accelerating wear and tear. To mitigate this issue, grooves are added to the pulleys, and protective shields are implemented to maintain the tendon’s alignment with the pulley system.

### 2.2.5 Airtightness Enclosure

To maintain consistent performance in terms of stiffness, it is required that there is no air leakage from the bellows during the recurring hopping process. Additionally, the bellows must withstand high air pressure to attain a greater degree of stiffness, so it’s significant to tackle the airtightness challenge.

In our design, we incorporate 3D-printed parts for establishing connections. However, these parts are generally not airtight by nature. To mitigate this, we adopt a 100% infill rate with a rectangular pattern in the 3D printing settings and an increased number of shell layers to diminish the occurrence of printed gaps. Moreover, we apply a specialized coating material to the surface of the part, which is adept at filling minor gaps between the filaments. After attaching the bellows to the 3D-printed plate, any residual gaps are filled using silicone, which is also used to coat the threaded joint.

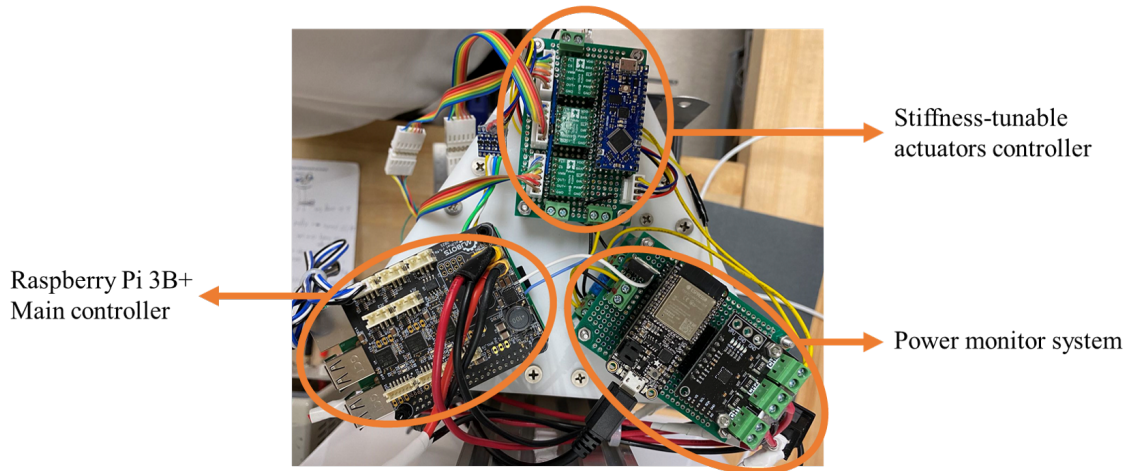


Figure 2-9: Electronics on the hopper top plate.

Despite these measures, it is challenging to completely eradicate gas leakage. Under high-pressure conditions, tiny fissures may form on the silicone surface of the bellows, leading to minor gas escape. Nevertheless, the velocity of leakage is so diminutive that we temporarily disregard this issue for the current stage of our research. Future studies could explore the employment of alternative materials as a potential solution to this problem.

## 2.3 Electronics

Electronics can be categorized into various subsystems, namely computation, communication, and sensing.

The computational subsystem is inclusive of the control mechanism for Pololu motors and the U8 motor, along with data processing procedures for the encoder, Inertial Measurement Unit (IMU), and power sensors. This element forms the basis of our interaction with the motor components and how the data from the various sensors are processed.

Communication, as a subsystem, covers aspects of inter-device dialogues as well as the user-end data feedback and logging system. This subsystem facilitates the

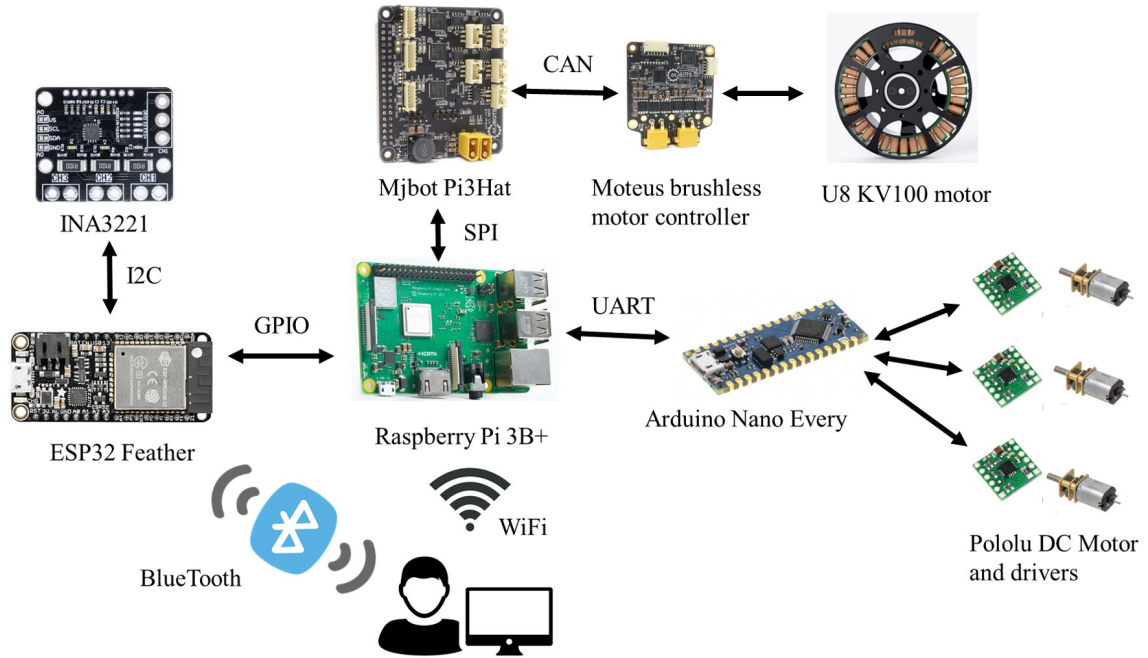


Figure 2-10: Electronic system diagram

interaction between devices and allows for effective data management and user-side feedback.

Lastly, the sensing subsystem embodies all the operations associated with sensors. This segment is critical for the collection and interpretation of real-time data, making it integral to the function and performance of the whole system.

The hopper employs three microcontrollers, namely the Raspberry Pi 3B+, Arduino Nano Every, and ESP32 Feather, as shown in Figure 2-9. Serving as the primary controller, the Raspberry Pi 3B+ is responsible for mathematical computations, managing the hopping behavior through the Mjbots robot control platform and motor driver, reading integrated IMU data during hopping, and transmitting commands to the subsequent level controller. Additionally, it communicates with the user's computer via WiFi.

In comparison to the Raspberry Pi, the Arduino Nano Every is equipped with a higher number of external interrupt pins, making it well-suited for simultaneously

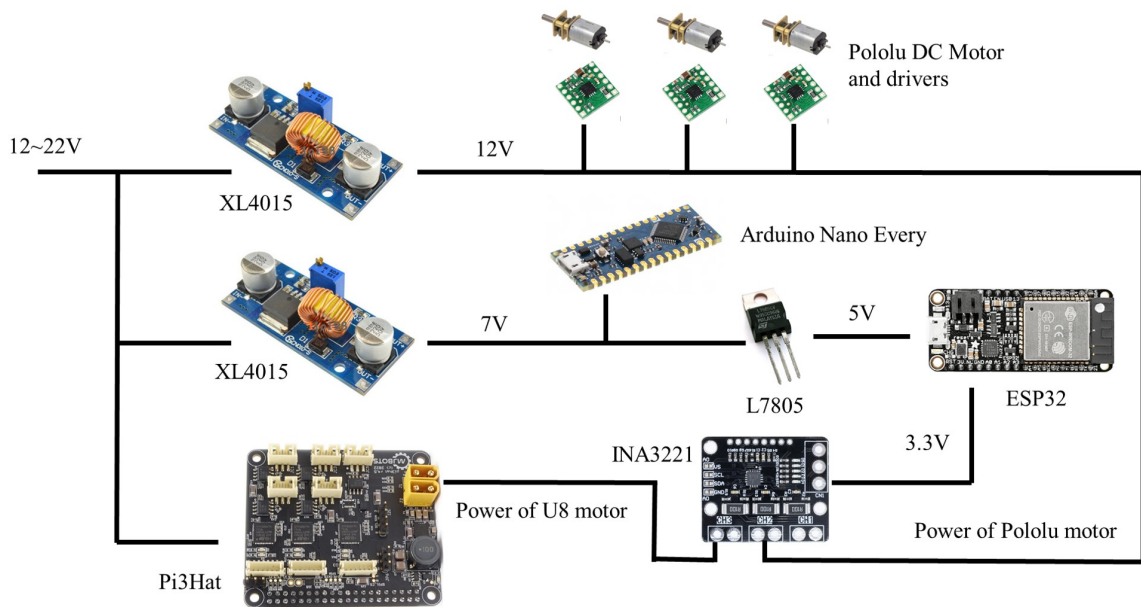


Figure 2-11: Power management System Diagram

reading multiple encoders and controlling the motors. The Raspberry Pi transmits the desired motor position through UART.

To facilitate real-time power consumption data transfer, the robot employs the ESP32 Feather, which features an embedded Bluetooth module. The power monitor module INA3221, operating in continuous mode, collects data that is subsequently read by the ESP32 via I2C. Ultimately, this data is plotted on the user's computer through a Bluetooth UART port. Therefore, with this hardware platform, we are able to achieve wireless control and data transmission.

The entire robot is powered by a DC power source, as illustrated in Figure 2-11. To safeguard the microcontrollers from voltage and current fluctuations, it is imperative not to connect the power supply directly to the microcontrollers' power supply pins. Instead, the supply voltage must traverse several isolators and regulators, including the DC-DC buck converter XL4015, L7805 power regulator, and onboard power modulators. The power monitoring module, INA3221, measures the real-time power consumption of the DC brushless tendon-driven motor and the total energy expenditure of the three Pololu motors. The collected data is then packaged and

transmitted to the ESP32 Feather via I2C.

During the rapid reciprocating motion of the motor, voltage spikes may occur on the power supply bus, a phenomenon known as "back electromotive force" (back EMF). These spikes result from the abrupt collapse of the motor windings' magnetic field when the current is interrupted or reversed. Given that the INA3221 can withstand a maximum voltage of 26V, it is crucial to eliminate these spikes to protect the circuits. Flux braking, which dissipates excess energy through an external resistor, serves as an effective solution to this issue.

## 2.4 Software

For continuous hopping to be achieved, the energy input must be equal to or greater than the energy loss in each hopping cycle. The hopper controller incorporates four states, as depicted in Figure 2-9, and utilizes a PID positional controller. During the initialization phase, the hopper applies minimal torque to tighten the spring and establishes the natural length of the tendon. The initiation of the hopper's operation and its transition into the flight phase are contingent on the detection of freefall. This detection is accomplished by monitoring the acceleration along the z-axis using the Inertial Measurement Unit (IMU) sensor. Within the program, a threshold is established to assist in the determination of the hopper's status. Specifically, freefall is registered when the z-axis acceleration falls below  $-15m/s^2$ . Alternatively, if the acceleration exceeds  $25m/s^2$ , an impact event is recognized by the program.

The controller's functionality is presented in the Algorithm 1, there are four states enumerated: initialization, flight, stance, and static, as shown in Figure 2-12. In the initial phase(line 4), the hopper will tighten the tendon and reset its natural length every time it runs the program. When a free fall is detected, the robot will goes into flight state. In the flight phase(line 9), the tendon stretches and compresses the spring, concurrently storing energy within the system. Upon impact detection, the system goes into the stance phase(line 13) where the tendon releases and the spring returns

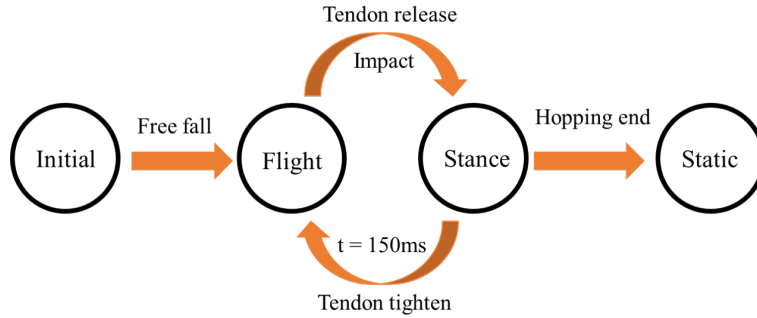


Figure 2-12: State machine of controller.

to its original length. After a constant predetermined impact duration has elapsed, the controller reverts to the flight state. considering the practical impact time and preventing duplicate detection, the predetermined impact duration is set to 150ms. This process results in consecutive jumps until the robot reaches a predetermined number of jumps and enters static mode(line 23). The motor is gradually reset to avoid tendon entanglement.

It is important to note that during our initial vertical hopping experiment, the spring stiffness remains constant throughout each test. The PID parameters are also kept constant to assure the hopping performance is constant during each test. However, the pre-compression length is changing base on the energy amount required for the system.

---

**Algorithm 1** Continuous Hopping Control Algorithm

---

**Require:** hopper, IMU sensor, and motor

**Ensure:** Continuous hopping for  $n$  times

```
1: State = enum(initialization=0, flight=1, stance=2, static=3)
2: Impact num = 0
3: while True do
4:   if State = initialization then
5:     Initialize hopper with minimal torque and natural tendon length
6:     if free fall is detected via IMU then
7:       State = flight
8:     end if
9:   else if State = flight then
10:    Stretch tendon and compress spring, storing energy
11:    Monitor IMU sensor for impact detection
12:    if Impact detected then
13:      State = stance
14:      Impact num = Impact num + 1
15:      if Impact num  $\geq$  Max Impact then
16:        State = static
17:      end if
18:    end if
19:   else if State = stance then
20:    Release tendon, allowing spring to return to the original length
21:    Wait for predetermined impact duration
22:    Set current state to flight
23:   else if State = static then
24:    Reset motor gradually to avoid tendon entanglement
25:   end if
26: end while
```

---

## 2.5 Future Improvements

On the mechanical side, our next step is to reduce the height of the hopper, and place the motor at the middle plate to lower the center of mass of the hopper, which makes it easier for balancing and controlling. Also, the threaded joint will be replaced by a barbed hose and pipe connection, which provides a more reliable seal.

The hose connection also allows the air chamber and spring to be offset, providing a design-level decoupling of these elements, and it streamlines the process of disassembling or replacing the parts. Moreover, the offset allows for a smaller size of leg which enable it to access larger orientation space.

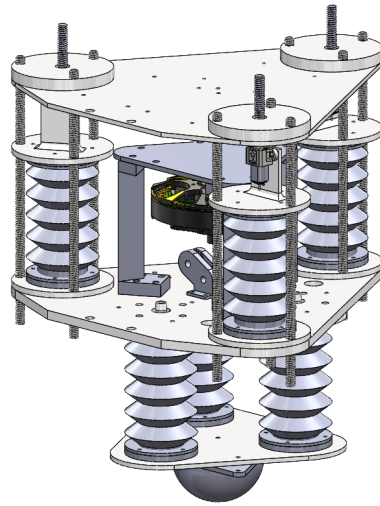


Figure 2-13: Next version of hopper.

# Chapter 3

## Bellows Model

In this chapter, we will elucidate the mathematical model that describes and forecast the behavior of the bellows actuator. The results derived from the simulation and their comparison with empirical data will be presented in the following sections.

### 3.1 Model of Air Chamber and Spring System

In the actuation system, both the air chamber and spring adopt a bellows-like structure, connected via a conduit. Each bellow can be modeled as an assembly of several segments, where each segment is formed of two conical frustra of opposite orientations. The air chamber has segment count  $n_c$ , frustra height  $h_c$ , inner radii  $R_c$ , and outer radii  $r_c$ . An identical representation approach is employed for the bellow spring, with the subscript  $s$  signifying the corresponding parameters.

For this idealized model, the assumptions made are that there is no expansion on the wall during the compression and release operations, and that the volume at the point of connection between the chamber and the spring is insignificant. The volume of the bellow is represented as a function of its height, yielding the following equations for the volumes of the air chamber and spring:

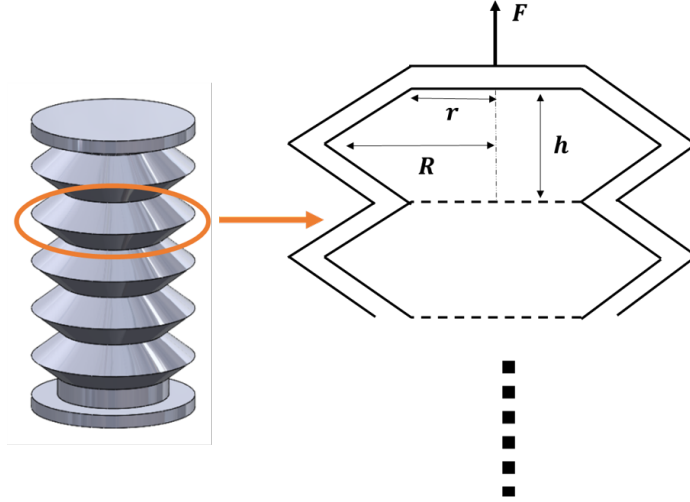


Figure 3-1: Air chamber and spring model

$$V_c(h_c) = \frac{2}{3}\pi n_c h_c (R_c^2 + r_c^2 + R_c r_c) \quad (3.1)$$

$$V_s(h_s) = \frac{2}{3}\pi n_s h_s (R_s^2 + r_s^2 + R_s r_s) \quad (3.2)$$

Considering the initial volumes of the air chamber  $V_{c0}$  and spring  $V_{s0}$ , and  $P_0$  as the standard atmospheric pressure, the present pressure,  $P_1$ , is derived from the ideal gas law as:

$$P_1(h_c, h_s)[V_c(h_c) + V_s(h_s)] = P_0(V_{c0} + V_{s0}) \quad (3.3)$$

Given that the work done by the change in gas volume is equivalent to the work executed by force displacing the bellow ( $PdV = Fdy$ ), the force generated by the gas is calculated as:

$$F_{gas}(h_c, h_s) = [P_1(h_c, h_s) - P_0] \frac{d[V_c(h_c) + V_s(h_s)]}{2n_2 dh_2} = [P_1(h_c, h_s) - P_0] \frac{\pi}{3} (R_s^2 + r_s^2 + R_s r_s) \quad (3.4)$$

An increase in pressure prompts the spring bellow to expand. However, the bellow's own structure constrains this expansion until the system attains equilibrium. Experiments indicate that the predominant expansion occurs along the length of the bellow, with minor lateral expansion. The elongation is determined by the following force balance equation:

$$F_{gas}(h_c, h_s + e) = e \cdot k_b \quad (3.5)$$

Where  $e$  denotes the spring elongation and  $k_b$  is the bellow stiffness.

It is observed that as the elongation effect mitigates pressure, there is a corresponding reduction in force, which concurrently results in a decrease in the stiffness range. To attain a higher level of stiffness, the bellow must withstand deformation under significant pressure, necessitating a more rigid bellow. Nonetheless, a stiffer bellow tends to have a lower stiffness range, thereby presenting a trade-off scenario.

## 3.2 Bellow Stiffness Measurement and Analysis

In this section, we conducted a series of experiments to investigate actuator and ground properties, which is the basis of the next chapter's energy analysis.

In the preceding section, the model that predicts the actuator's stiffness was described. The spring bellow's stiffness can be manipulated through the displacement of the air chamber, which is a function of the air pressure, and an increase in pressure corresponds to an increase in spring stiffness.

In the prototype, the air chamber and spring have identical dimensions. The specific parameters pertaining to the bellow segments are summarized in Table 3.1. This set of parameters was designed as the optimal parameter based on experiments, taking into account stiffness range, stability, size, and shape. Generally, a bellow with less segment amount, wider diameter, and a smaller difference between the large radius and the small radius will be more stable.

Segment height $h$	Large Radius $R$	Small Radius $r$	Segment Amount $n$	Thickness $t$
7.46mm	20.10mm	10.58mm	5	3mm

Table 3.1: Bellow design overview

We use a Material Testing System (MTS) machine to determine the stiffness. The leg, composed of three springs, was inverted on the test plate. To ensure a level top plate, all three air chambers had to undergo identical compression. To eliminate the impact of damping effects, the velocity for the stiffness test was set at 1mm/s. The MTS compression length is set to 20mm which can circumvent the potential bellow buckling issues. Each test of the same compression length would be repeated 3 times to ensure the accuracy of the results.

The results of the test are depicted in Figure 3-3a and the raw data were listed in Table 3.2. Due to both elongation and buckling problems in the bellows, the practically achievable pressure range is narrower than the theoretical range. The experimental setup is illustrated in Figure 3-2. The observed discrepancy might be attributed to irregular expansion at the wall. Notably, the actual expansion also occurs on the sidewalls, leading to wall deformation. This deformation can reduce the pressure, subsequently decreasing the output force.

In Figure 3-3b, the variation in stiffness with increasing air chamber compression is depicted. This stiffness is derived through a linear fit of the force-displacement curve, as shown in Figure 3-3a. The graphical representation illustrates a trend of increasing stiffness for an equivalent increment in compression, which can be interpreted as an increase in the corresponding pressure. The error bars, signifying the standard deviation from three repeated tests, endorse the good reproducibility of these results.

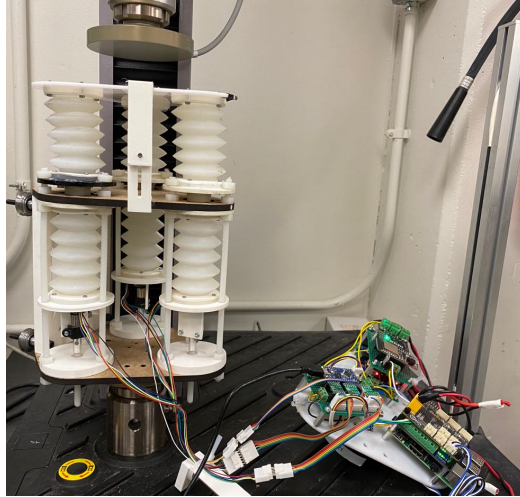


Figure 3-2: Hopper leg stiffness test scenario.

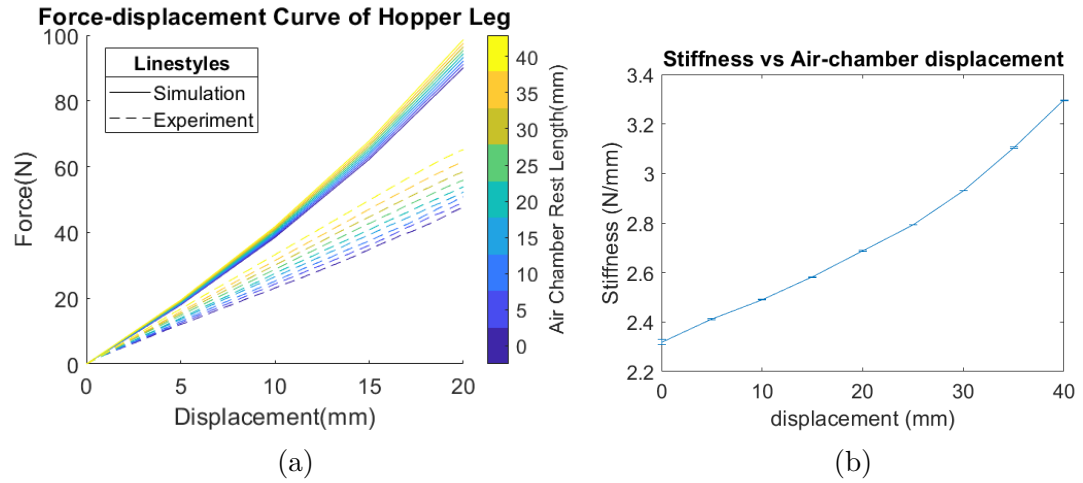


Figure 3-3: (a) Simulation and experiment comparison. (b) stiffness changing with respect to air chamber displacement.

Table 3.2: Hopper stiffness MTS test result

Air Chamber Compression (mm)	Stiffness (N/mm)			Average Stiffness(N/mm)	Standard Deviation (N/mm)
0	2.308	2.324	2.327	2.320	0.010
5	2.409	2.413	2.414	2.412	0.002
10	2.488	2.490	2.492	2.490	0.002
15	2.581	2.583	2.582	2.582	0.001
20	2.692	2.686	2.686	2.688	0.003
25	2.791	2.794	2.793	2.793	0.001
30	2.932	2.931	2.930	2.931	0.001
35	3.103	3.105	3.107	3.105	0.002
40	3.297	3.295	3.294	3.295	0.001

The findings suggest that the stiffness of the hopper leg can be modulated by approximately 1.42 times, ranging from 2319N/m to 3295N/m with good linearity in the process.

# Chapter 4

## Robot Model

In the present chapter, the focus shifts to the explication of models for both the hopper leg and the hopper-ground system. Proceeding from the elucidation of the tunable-stiffness pneumatic spring actuator in the previous chapter, a more comprehensive exploration of the leg behavior, considered as an assembly of three springs, is presented. This chapter then proceeds to formulate a model of the hopper and the ground and simulate its hopping process. The simulated results are subsequently juxtaposed against corresponding experimental data to draw meaningful inferences.

### 4.1 Hopper Leg Model

The leg of the hopper is composed of three pairs of air chambers and springs, which collectively generate adequate force to propel the hopper and facilitate changes in its orientation. This model endeavors to predict the trajectory and attitude of the hopper leg during the central tendon retraction process, under the assumption that the volume of the air chambers remains invariant throughout.

Adhering to the principle that a closed system in the absence of external forces will naturally evolve towards a state of lower energy, the state of equilibrium can be framed as an optimization problem that seeks to minimize the energy of the system[32].

Presuming identical initial lengths  $l_0$  and total volumes  $V_0 = V_{s0} + V_{c0}$  for each spring, the lengths of the springs after the compression of the air chambers are denoted as  $l_1$ ,  $l_2$ , and  $l_3$ . Leveraging the ideal gas law, the potential energy of the gas in the three chamber-spring pairs is expressed as follows:

$$U_{gas} = \sum_{i=1}^3 \int_{V_i}^{V_0} P(V_i) dV_i = \sum_{i=1}^3 \int_{l_i}^{l_0} P(l_i) V'(l_i) dl_i = \sum_{i=1}^3 \frac{2}{3} (R_s^2 + r_s^2 + R_s r_s) P_0 V_0 \int_{l_i}^{l_0} \frac{1}{V(l_i)} dl_i \quad (4.1)$$

This equation postulates that the internal energy of the gas can be represented as a function of the spring's length. The equation can be simplified to:

$$U_{gas} = c \cdot \ln \frac{(a_1 + bl_0)(a_2 + bl_0)(a_3 + bl_0)}{(a_1 + bl_1)(a_2 + bl_2)(a_3 + bl_3)} \quad (4.2)$$

where  $a, b, c$  are constants,  $a_i$  represents the volume of the chamber which remains constant,  $b$  is the spring volume constant, and  $c$  is the gas energy constant.

$$\begin{aligned} a_i &= \frac{2\pi}{3} n_c h_{ci} (R_c^2 + r_c^2 + R_c r_c) \\ b &= \frac{\pi}{3} (R_s^2 + r_s^2 + R_s r_s) \\ c &= P_0 V_0 \end{aligned} \quad (4.3)$$

Assuming that each bellow spring has the same stiffness  $k_b$ , the potential energy of the three springs can be denoted as:

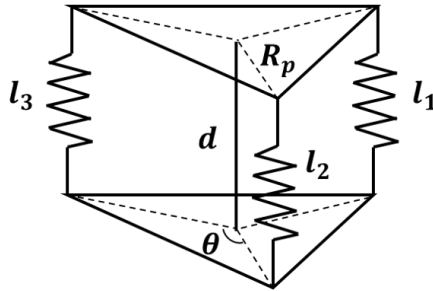


Figure 4-1: Hopper leg model

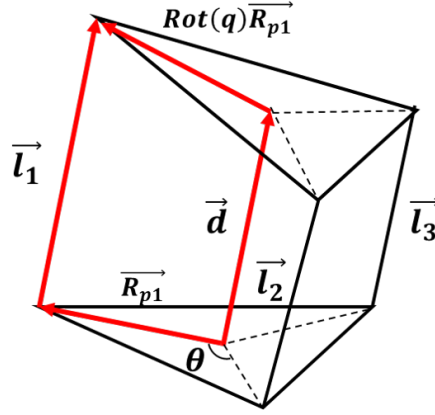


Figure 4-2: Hopper leg model

$$U_{spring} = \frac{1}{2}k_b[(l_0 - l_1)^2 + (l_0 - l_2)^2 + (l_0 - l_3)^2] \quad (4.4)$$

To derive the state of equilibrium by minimizing the energy, we can construct the objective as the energy function, subject to geometrical and tendon constraints. The optimization problem is constructed as follows:

$$\begin{aligned} \min_{x,y,z} \quad & U_{gas} + U_{spring} \\ \text{s.t.} \quad & l_i = T - \frac{2R_p}{T}(x \cos\theta_i + y \sin\theta_i), \quad i = 1, 2, 3 \\ & T^2 = x^2 + y^2 + z^2 \end{aligned} \quad (4.5)$$

where point  $(x, y, z)$  is the center of the top plate, with the origin at the center of the bottom plate.  $T$  is the length of the central tendon. Upon determining the lengths  $l_i$  of each spring, the structure of the hopper leg can be recreated leveraging the geometric principles of the model. For the purpose of elucidating the analysis, the hopper leg is depicted in an inverted position as illustrated in Figure 3-5. The toe, situated at the center of the top plate, has its orientation defined by the lengths of the three springs.

With the center of the bottom plate as the origin, three vertices can be written

as[32]:

$$\vec{l}_i = \vec{T} + Rot(q)\vec{R}_{pi} - \vec{R}_{pi} \quad (4.6)$$

where  $q = [\frac{z}{T}, \frac{y}{T}, \frac{x}{T}, 0]$  is the quaternion of top plate orientation.  $Rot(q)$  is the rotation matrix converted from  $q$ , which is:

$$Rot(q) = \begin{bmatrix} 1 - 2(\frac{y}{T})^2 & 2(\frac{y}{T})(\frac{x}{T}) & 2(\frac{z}{T})(\frac{x}{T}) \\ 2(\frac{y}{T})(\frac{x}{T}) & 1 - 2(\frac{x}{T})^2 & 0 \\ 2(\frac{z}{T})(\frac{x}{T}) & 0 & 1 - 2(\frac{x}{T})^2 - 2(\frac{y}{T})^2 \end{bmatrix} \quad (4.7)$$

## 4.2 Hopper Leg Simulation

This simulation was performed based on the model proposed in Section 3.2. Given the compression of the three air chambers, we build a simulation program to predict the attitude of the bottom plate when the tendon is pulling. In Figure 4-3, a three-dimensional depiction of the energy function of the hopper leg is presented, given the condition that all three air chambers share equivalent pre-compression. It can be observed from the graphical representation that the function exhibits convexity, a property consistent with theoretical expectations. Furthermore, the point of minimal energy can be identified around coordinates (0,0), a finding which aligns with empirical results obtained from our experimental study.

Figure 4-4 illustrates the changes in position and orientation of the bottom plate as the tendon is pulling. The colors indicate the states during which the bottom plate is pulled by the tendon. The scatter points at the middle delineate the trajectory of the bottom plate's center where the tendon is attached.

The simulation findings suggest that the energy optimization problem is convex and solvable, eventually converging to a stable state with the minimum energy. However, due to time constraints, we have not yet performed experiments to validate this model. In the near future, we plan to utilize a 3D motion capture system to gather data and conduct hopping experiments within a three-dimensional space.

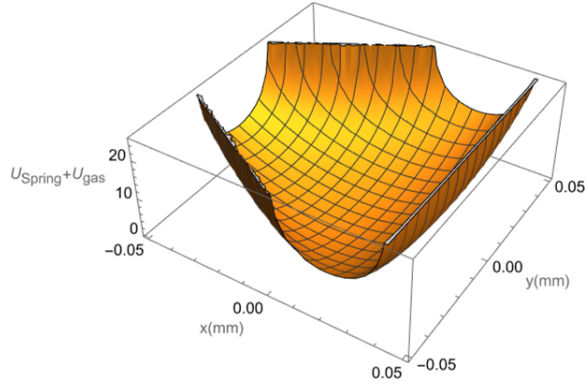


Figure 4-3: Convexity of energy function.

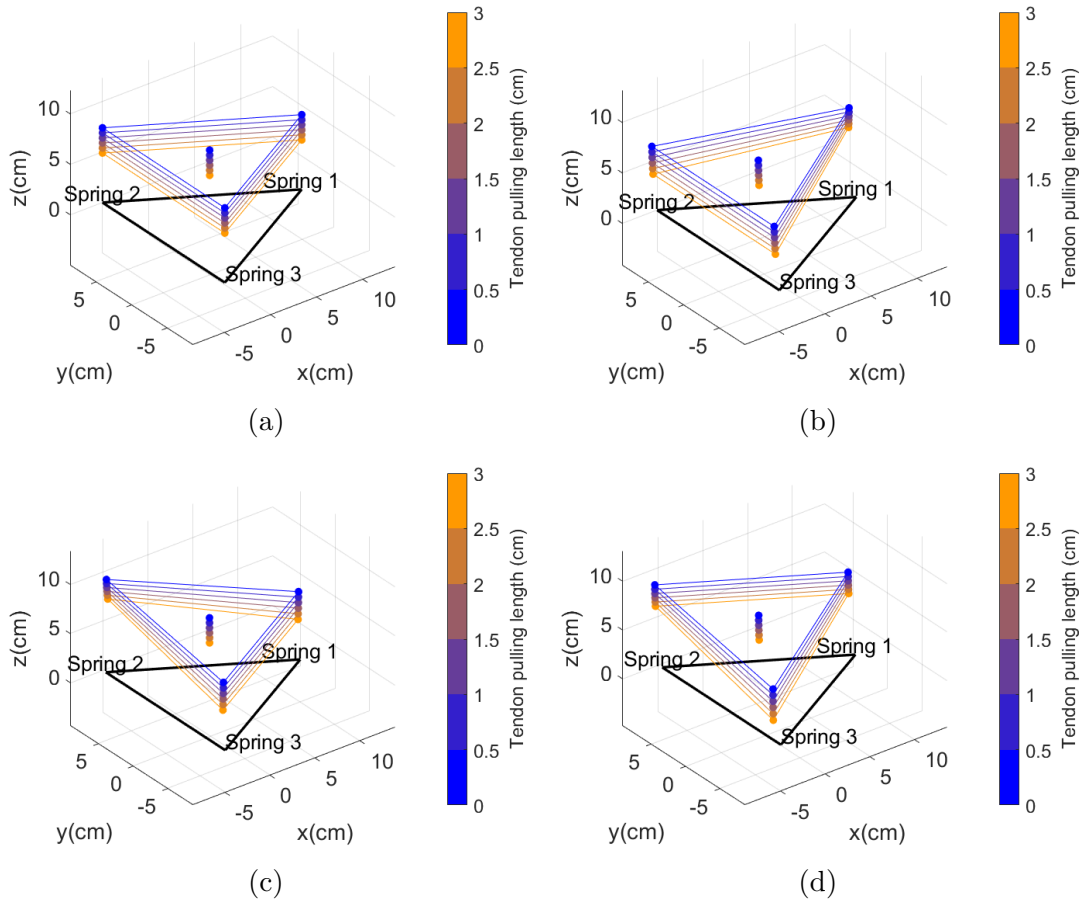


Figure 4-4: Bottom plate orientation and trajectory when tendon pulling for 30mm. Each figure corresponds to an initial actuator state: (a)  $[0\ 0\ 0]$ , (b)  $[4\ 0\ 0]$ , (c)  $[0\ 4\ 0]$ , (d)  $[4\ 4\ 0]$ , where each element in the  $1 \times 3$  matrix pertains to a respective air-chamber compression in millimeters.

### 4.3 Hopper Dynamics Model

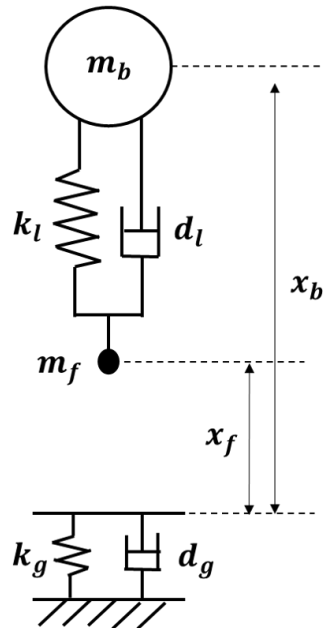


Figure 4-5: Hopper model

The model depicted in Figure 4-5 portrays both the hopper and the ground as spring-damping systems, characterized by a leg spring stiffness  $k_l$  and a damping coefficient  $d_l$ , the ground uses the same notation with the subscript  $g$ . To sustain a continuous hopping motion, the hopper requires the 'pre-compression' of its leg whilst airborne and its subsequent full release upon ground impact. In this model, The weight of the hopper's leg is denoted as  $m_f$ , with its natural length and pre-compression length represented by  $L$  and  $p$ , respectively. The hopper's body weight is symbolized as  $m_b$ . A complete jumping cycle can be partitioned into four distinct phases, each of which is expounded upon in Figure 4-6. The hopper controller state machine is depicted in Figure 4-7:

1. initial phase: The hopper starts at zero velocity and free falls until it impacts the ground( $x_f = 0$ ).

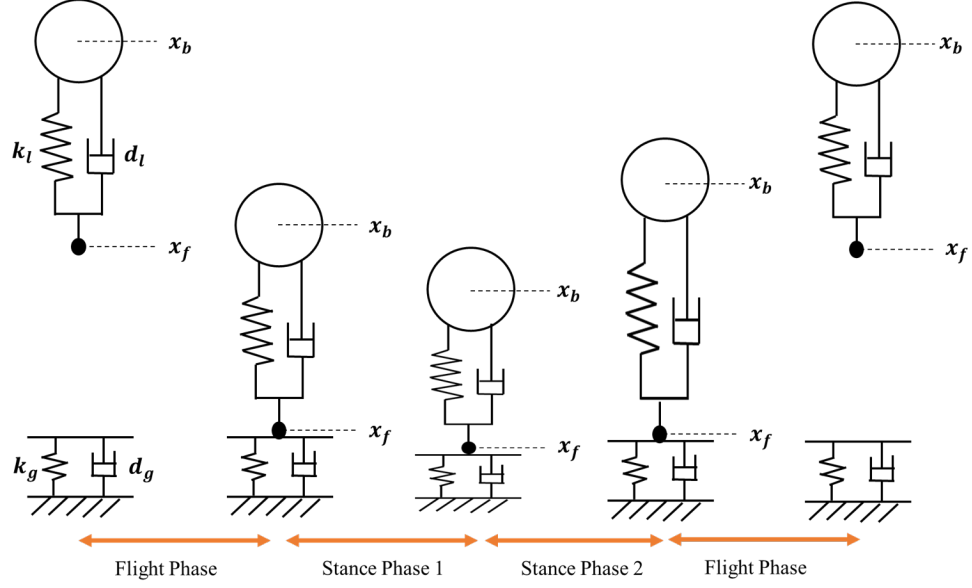


Figure 4-6: Phases of hopping

Model:

$$\begin{aligned}\ddot{x}_b &= g \\ \ddot{x}_f &= g\end{aligned}\tag{4.8}$$

2. Stance phase 1: Starting from an impact detection, the hopper's body's height continues reducing until reaches the minimum height ( $\dot{x}_b = 0$ ).

Model:

$$\begin{aligned}F_l &= k_l(l - p - x_b + x_f) - d_l(\dot{x}_b - \dot{x}_f) \\ F_g &= -k_g x_f - d_g \dot{x}_f \\ m_b \ddot{x}_b &= F_l - m_b g \\ m_f \ddot{x}_f &= -F_l + F_g - m_f g\end{aligned}\tag{4.9}$$

3. Stance phase 2: Start with positive hopper body speed, meanwhile the spring is fully released. This phase ends with the hopper toe leaving the ground ( $x_f > 0$ ).

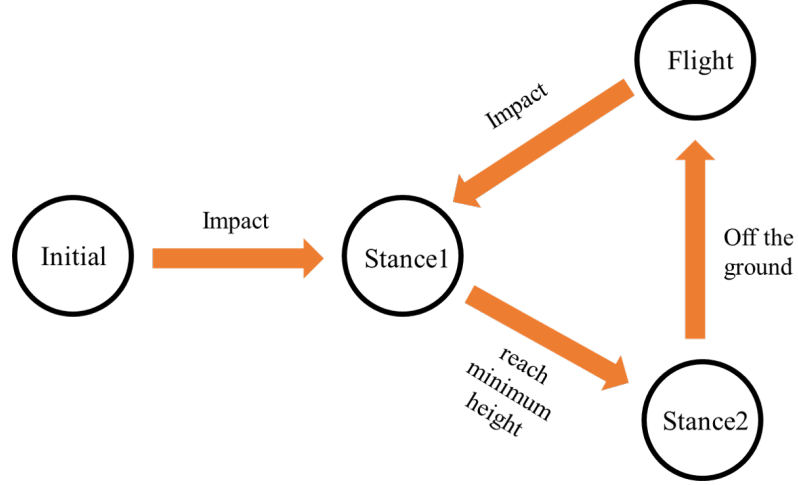


Figure 4-7: State machine of the model

Model:

$$\begin{aligned}
 F_l &= k_l(l - x_b + x_f) - d_l(\dot{x}_b - \dot{x}_f) \\
 F_g &= -k_g x_f - d_g \dot{x}_f \\
 m_b \ddot{x}_b &= F_l - m_b g \\
 m_f \ddot{x}_f &= -F_l + F_g - m_f g
 \end{aligned} \tag{4.10}$$

4. Flight phase: The hopper continues rising until the body velocity reduces to zero ( $\dot{x}_b = 0$ ). The leg spring may still vibrate in the air.

Model:

$$\begin{aligned}
 F_l &= k_l(l - p - x_b + x_f) - d_l(\dot{x}_b - \dot{x}_f) \\
 m_b \ddot{x}_b &= F_l - m_b g \\
 m_f \ddot{x}_f &= -F_l + F_g - m_f g
 \end{aligned} \tag{4.11}$$

Within each hopping cycle, energy is lost due to spring damping. As previously mentioned, the 'pre-compression' process infuses energy into the system, thereby ensuring continuous hopper motion. In order to examine the comprehensive energy expenditure throughout the hopping process, which encompasses both damping and

spring potential energy, it is necessary to investigate the rate of change in energy over time.

The rate of energy dissipation to the ground during the stance phase is given by[19]:

$$\dot{E}_g = \frac{d}{dt} \int_0^{x_f} (k_g x_f + d_g \dot{x}_f) dx_f = k_g x_f \dot{x}_f + d_g \dot{x}_f^2 \quad (4.12)$$

The rate of energy loss to the hopper leg during the stance phase is:

$$\begin{aligned} \dot{E}_l &= \frac{d}{dt} \int [k_l(l - x_b + x_f) + d_l(\dot{x}_b - \dot{x}_f)] d(x_b - x_f) \\ &= k_l(l - x_b + x_f)(\dot{x}_b - \dot{x}_f) + d_l(\dot{x}_b - \dot{x}_f)^2 \end{aligned} \quad (4.13)$$

The energy injected into the system during each cycle is:

$$E_p = k_l \cdot p^2 \quad (4.14)$$

Theoretically, if the hopping height remains constant throughout a cycle, the energy gained and the energy lost to damping will always be equivalent.

## 4.4 Ground and Hopper Damping Measurement and Analysis

In order to substantiate the proposed model, this section discusses ascertaining the parameters of the system, which are subsequently utilized for simulation. The data collected includes ground stiffness and the damping coefficient for both the ground and hopper leg.

### 4.4.1 Ground Stiffness Measurement

The ground is modeled as a spring-damping system within the hopper-ground model. We selected three different materials, characterized by soft, medium, and hard stiffness, for ground testing. To mimic the force perceived by the hopper as accurately as possible, we employed a 3D-printed probe identical in size to the hopper's toe, as illustrated in Figure 4-8. The resulting data of stiffness is presented in Table 4.1. The materials selected for simulating the soft and medium ground consist of different types of foam, whereas the hard ground is represented by steel plate.

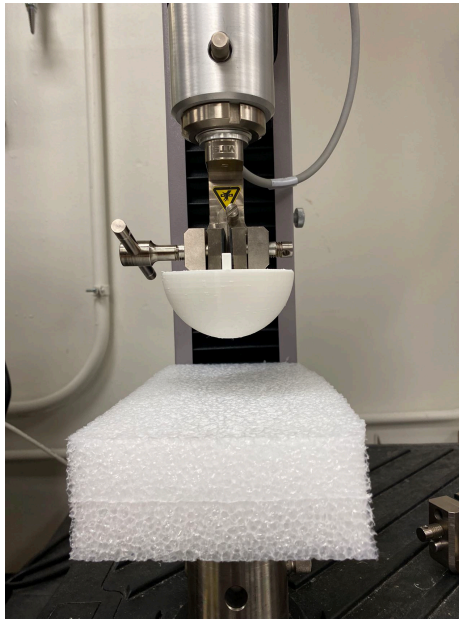


Figure 4-8: Toe-shape probe and ground material.

Table 4.1: Ground stiffness MTS test result

Material type	Stiffness Tests (N/mm)			Average Stiffness(N/mm)
Soft	2.095	2.187	2.068	2.117
Medium	15.250	15.533	15.485	15.423
Hard	> 10 <sup>6</sup>			

## 4.4.2 Damping Measurement and Analysis

The damping force is the primary factor contributing to energy dissipation. It is contingent upon both velocity and the damping coefficient. Owing to the complexity of damping mechanisms, quantifying this material property poses a significant challenge. In our experiment, we employ two different strategies to measure the damping coefficient.

The first and most direct approach involves using an MTS machine to perform a compression test at a specified velocity. However, this method has its constraints. The displacement length, restricted to 2cm for the hopper leg, is insufficient for the MTS machine probe to undergo the acceleration and deceleration process, thus introducing errors into the results. Furthermore, for materials with lower damping coefficients, differentiating the damping from other energy-dissipating effects, such as friction, requires testing across a range of velocities. However, the probe cannot achieve high velocities within such a short timeframe, rendering the results less distinguishable.

An alternative approach entails measuring the damping force via height attenuation in a free-falling object test. To measure the ground's damping coefficient, a static ball is dropped and its bouncing height recorded, thereby enabling precise calculation of the velocity at the moment of impact and liftoff. Compared to unidirectional compression, an elastic collision in a compression-rebound process conserves kinetic energy and momentum, implying that the primary energy loss is due to the damping effect.

In the floor damping measurement experiment, we use a ball with the same dimensions as the hopper toe. This ball is 3D-printed and remains undeformed during impact. After being dropped onto the ground material, the ball bounces back to a certain height, a process captured by a 240 fps high-speed slow-motion camera. The trajectory is then analyzed using the video analyzer "tracker", which employs vision techniques to extract a specific color block or marker.

The damping force, contributing to momentum loss during impact, can be calcu-

lated to determine the damping coefficient. Assuming a ball mass of  $m$  and an impact time of  $t$ , the damping force  $F_{damping}$  is given by:

$$F_{damping} = \frac{m\Delta V}{t} \quad (4.15)$$

Here,  $\Delta V$  is derived from the initial height  $h_1$  and the subsequent height  $h_2$ , and it's an absolute value:

$$\Delta V = \sqrt{2gh_1} - \sqrt{2gh_2} \quad (4.16)$$

Here we assume that the force applied to the ball remains constant. To calculate the damping force within the brief duration of impact, we utilize the average velocity as a substitute for instantaneous velocity. The damping coefficient, denoted by  $c$ , is subsequently computed by dividing the damping force by the average velocity. This average velocity is calculated based on the absolute velocity observed at the points of impact and lift-off.:

$$c = \frac{F_{damping}}{V_{avg}} = \frac{2m(\sqrt{2gh_1} - \sqrt{2gh_2})}{t(\sqrt{2gh_1} + \sqrt{2gh_2})} \quad (4.17)$$

The test scenario exemplification, along with the video tracker data visualizations, is depicted in Figure 4-9 and 4-10. In the ground damping experiment, a 3D-printed rigid ball is employed to carry out drop tests on various ground surfaces. Conversely, the damping coefficient of the hopper leg is examined through a series of free drop tests of legs with differing stiffness onto a rigid metal ground. Each screenshot is accompanied by a timestamp, which is also indicated on the plot. After offset elimination, the ground position is normalized to zero. To accurately determine the impact time, the data collected is interpolated to find the point of intersection on the x-axis. The peak values extracted from the graph correspond to the maximum jumping height.

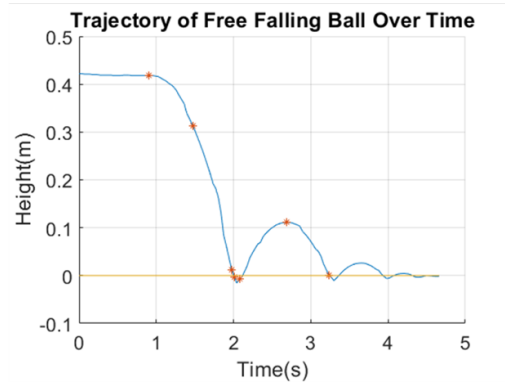
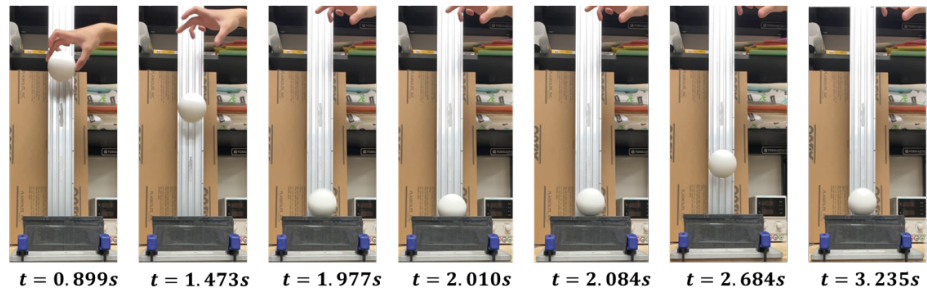


Figure 4-9: Ground damping test example.

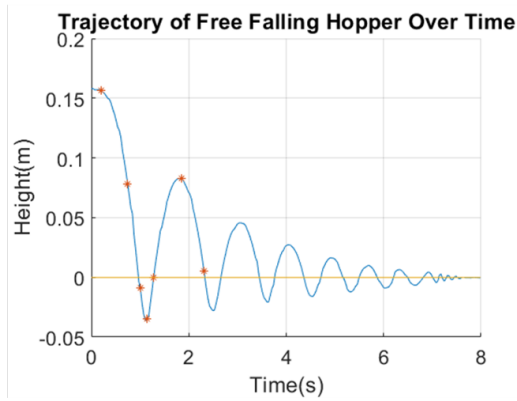
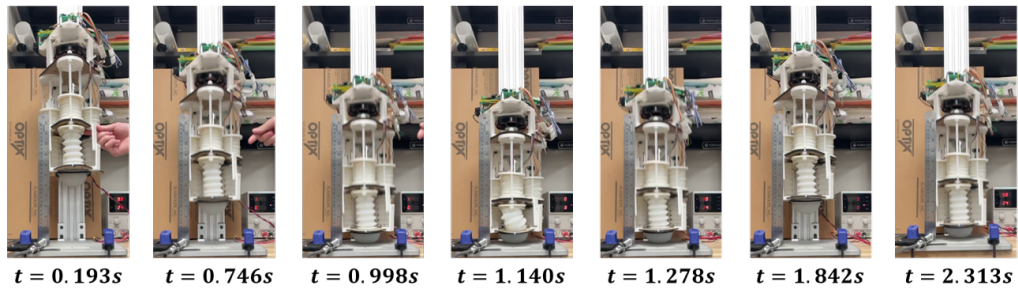


Figure 4-10: Hopper leg damping test example.

The damping tests for each set encompass three trials at distinct drop heights,

with results delineated in Tables 4.2. The terms "Soft leg" and "Hard leg" refer to the hopper's leg at its minimum stiffness of 2320 N/m and maximum stiffness of 3295 N/m, respectively. "Soft" and "Medium" ground, as listed in Table 4.1, represent different ground materials characterized by varying stiffness.

In the experimental configuration, a metal track marked 20cm, 30cm, and 40cm above the ground serves as the reference for the respective low, medium, and high drop heights in the dropping height column. Although the exact height varies slightly across tests, it is precisely ascertained through video tracking for data accuracy.

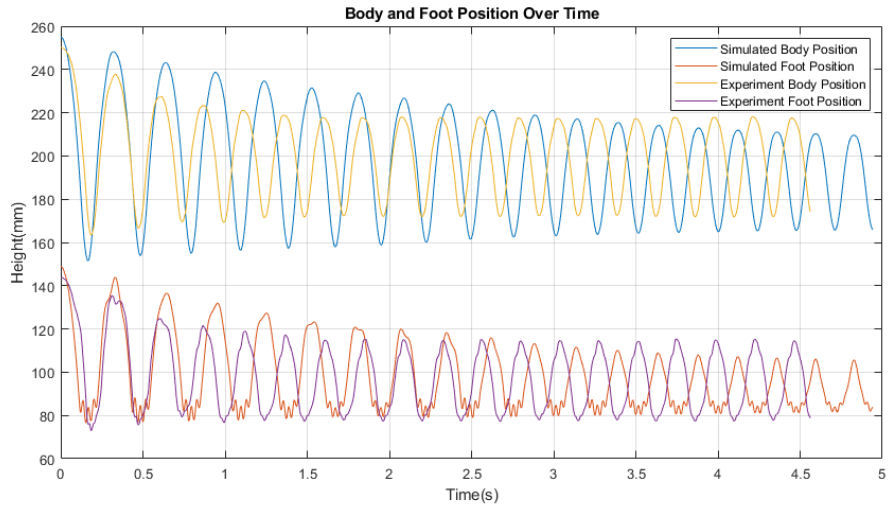
Table 4.2: Hopper leg damping test data

Test Material	Dropping Height	Leg Damping Coefficient (N*s/m)	Average Damping Coefficient (N*s/m)	Standard Deviation (N*s/m)
Soft Leg	Low	2.22	2.83	0.54
	Medium	3.03		
	High	3.25		
Hard Leg	Low	2.79	2.54	0.22
	Medium	2.42		
	High	2.39		
Soft Ground	Low	0.38	0.41	0.03
	Medium	0.44		
	High	0.42		
Medium Ground	Low	0.43	0.48	0.09
	Medium	0.57		
	High	0.42		

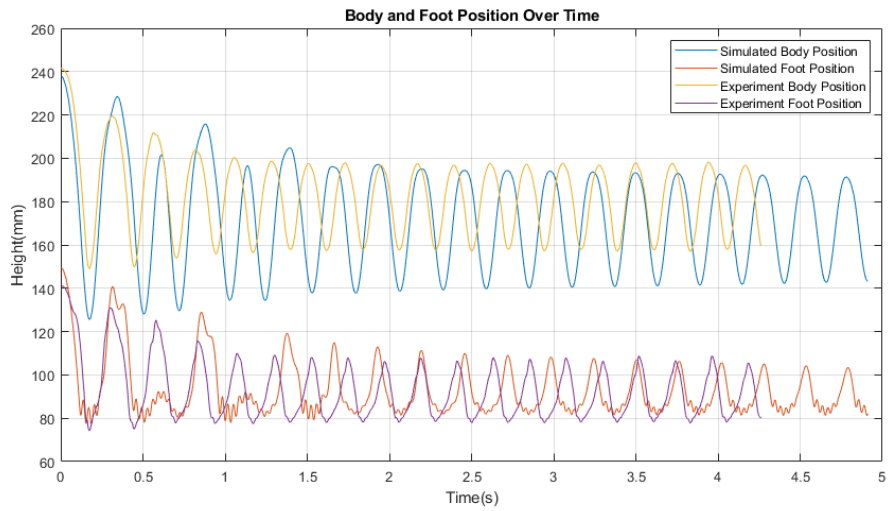
## 4.5 Hopper Dynamics Simulation

In this empirical investigation, the hopper is configured to release from a designated height above the ground, and the simulation deploys identical parameter settings except for the pre-compression, which governs the energy input into the system. The pre-compression in the simulation is prescribed as 1.5mm for the softer leg (with a stiffness of 2320N/m) and 0.8mm for the stiffer leg (3295N/m). The comparative figures incorporate the visual tracking data of both the hopper body and foot, and the simulated trajectory with an offset for the actual hopper structure. No tests were conducted on the hard ground because an extremely hard material is incompatible with the spring-damping model. Thus, testing was limited to medium ground (15423N/m) and soft ground (2117N/m). The testing process was continued for 19 impacts, as illustrated in Figure 4-11 and Figure 4-12.

While the graph demonstrates certain relationships between the simulation and the experimental data, a considerable discrepancy is observed in terms of pre-compression and time expenditure. This gap in pre-compression signifies that the model is idealistic, accounting only for damping energy loss. In contrast, in a realistic experimental setup, energy loss may be attributed to multiple sources such as wheel friction, pulleys friction, leg regulators friction, collisions, motor flux braking heat dissipation, energy loss in bellow buckling, among others. The time discrepancy noted in Figure 4-12 suggests that the model underestimates the energy dissipation on soft ground. This is indicated by the fact that a lower jumping height would naturally lead to a shorter duration.

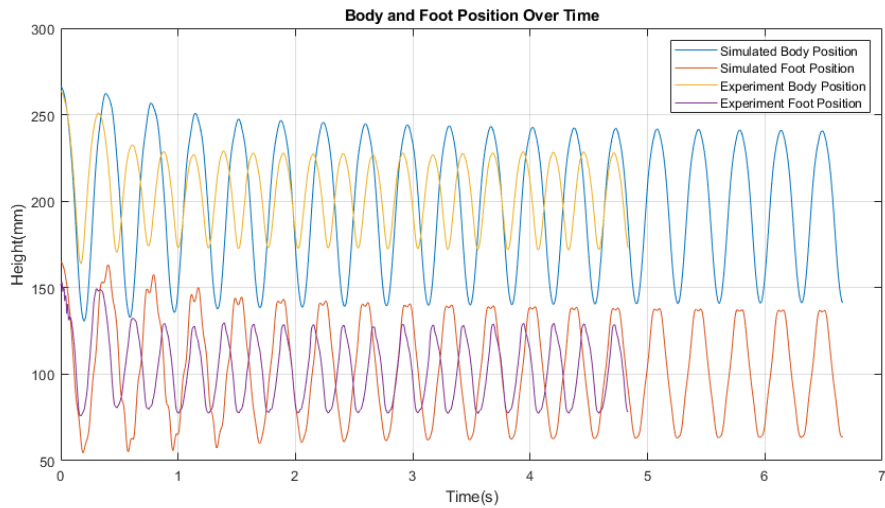


(a)

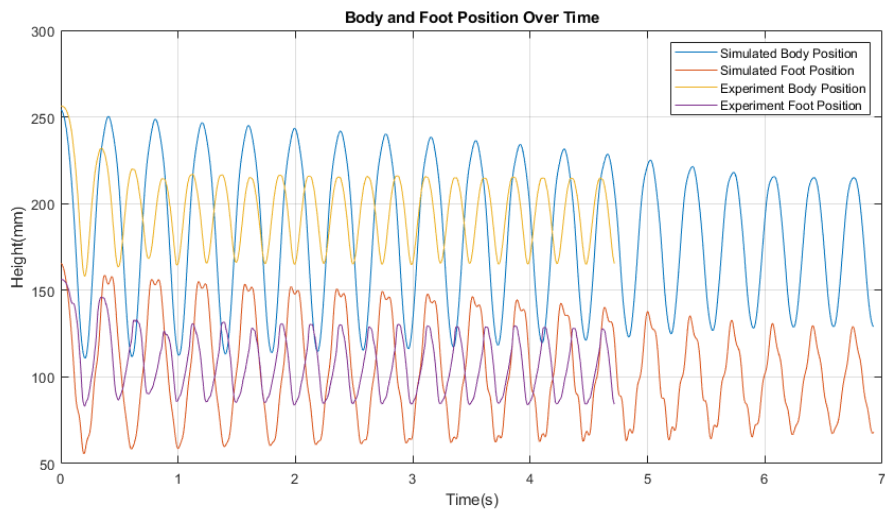


(b)

Figure 4-11: Tests on the medium ground. (a) Hopping with soft leg. Actual and simulated pre-compression(mm): 37, 1.5. (b) Hopping with hard leg. Actual and simulated pre-compression(mm): 33, 0.8.



(a)



(b)

Figure 4-12: Figure 4-11: Tests on the soft ground. (a) Hopping with soft leg. Actual and simulated pre-compression(mm): 56, 1.5. (b) Hopping with hard leg. Actual and simulated pre-compression(mm): 53, 0.8.

# Chapter 5

## Hopper Energy Efficiency Analysis

This chapter analyzes the energy cost during the hopping and proposes a compliance matching strategy base on the simulation result. We also conduct several experiments using the previously designed hopper with a stiffness-tunable leg to verify the theory and get the conclusion.

### 5.1 Energy Cost of Altering Stiffness

In the actuation mechanism, the leg-driving actuation system and the tunable stiffness actuators are separately controlled, allowing for separate measurements. As represented in Equation 5.1, the energy expenditure  $E$  of the three tunable-stiffness actuators is integrated through the sum of respective motor power, which is current  $I_i$  multiplied  $V_i$ . These motors (specifically, Pololu 100:1 Micro Metal Gearmotor HPCB 12V) are affixed to the lead screw, facilitating the compression of the bellow.

$$E = \int_0^t \left( \sum_{i=1}^3 V_i I_i \right) dt \quad (5.1)$$

During the assessment, the motors share an identical desired position, and energy consumption is measured throughout a complete cycle, from the initiation to the return to the starting point. The findings are visually represented in Figure 5-1.

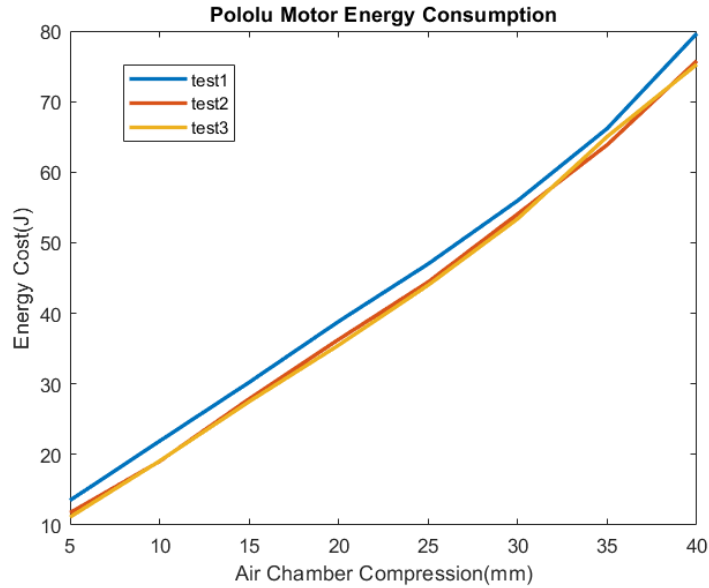


Figure 5-1: Pololu motor energy consumption

As the degree of compression increases, the energy required for attaining the same level of compression grows. This trend is attributed to the augmented air pressure which required more force.

## 5.2 Hopping Height Equilibrium

To substantiate the controllability of the hopping height, it is required to establish the correlation between tendon compression and the resultant hopping height. In the simulation delineated in Figure 5-2, parameters such as leg stiffness and tendon compression are held constant, while the hopper is introduced at varying heights. The simulation shows a limit cycle in the phase portrait, ultimately resulting in convergence towards an equilibrium height.

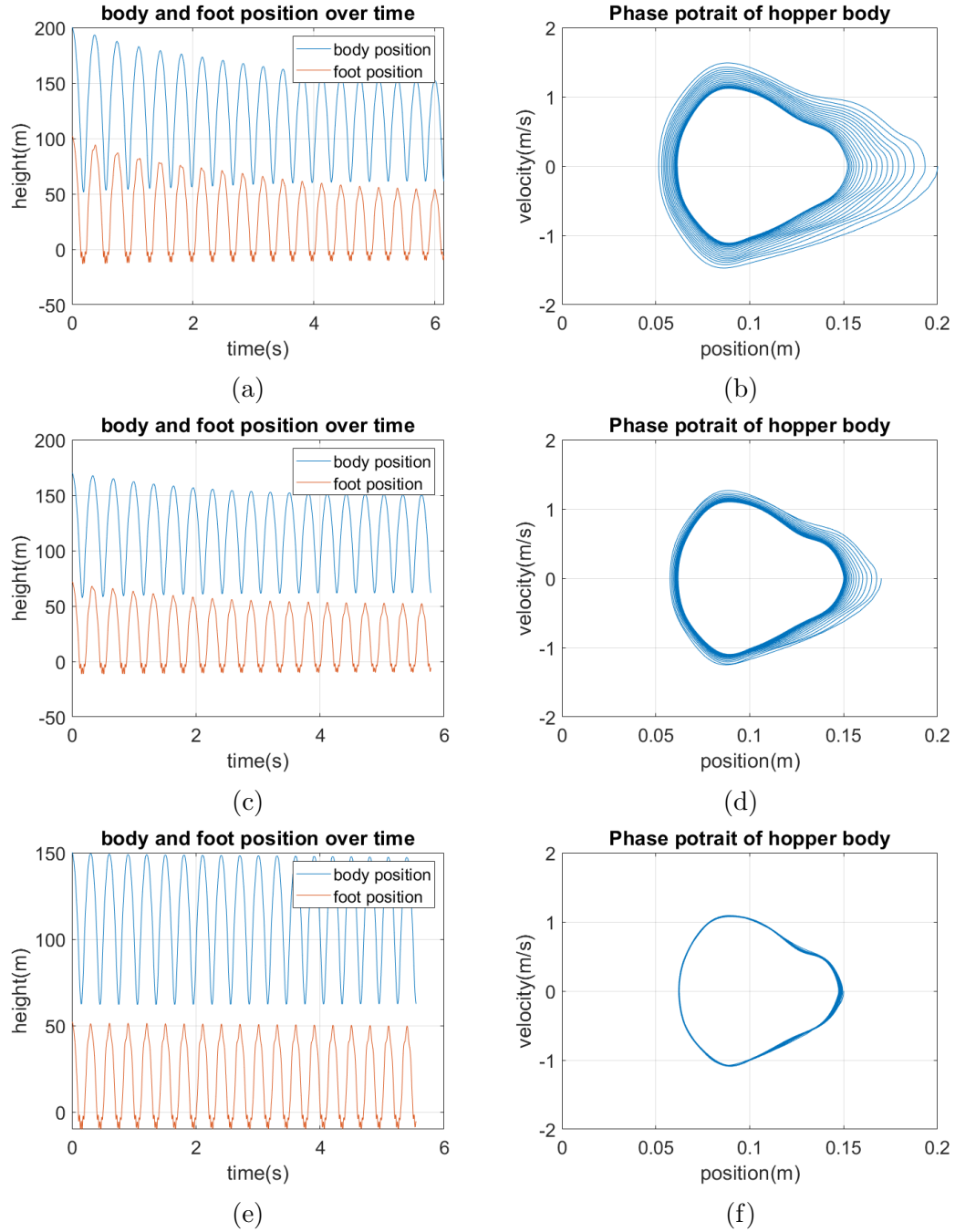


Figure 5-2: Simulation of Equilibrium Hopping Height. The left-hand side figures illustrate time-domain trajectories, while the right-hand side displays the phase portraits. Each pair of figures corresponds to a unique initial height from which the robot commences: (a,b) 200mm; (c,d) 170mm; (e,f) 150mm.

Simulated Parameters	Values
Spring rest length(m)	0.1
Body mass(kg)	1.5
Foot mass(kg)	0.25
Ground stiffness(N/m)	10000
Leg stiffness(N/m)	2600
Ground damping(N*s/m)	0.4
Leg damping(N/m)	2.5
Pre-compression(mm)	2

Table 5.1: Parameters of equilibrium height simulation.

The simulation result suggests that when the tendon compression is maintained at 2mm and spring stiffness remains constant during the hopping process, the hopping height eventually stabilizes around 150mm.

To empirically verify the existence of an equilibrium height, the hopper is discharged from various initial heights, and its body and foot positions are tracked utilizing a video tracker. The resultant tracking data are graphically delineated in Figure 5-3, where color is employed to denote the initial height from which the hopper descends. The experimental hopper parameters are detailed in Table 5.2. The result from trials substantiates the conjecture that a hopper, operating under consistent compression and stiffness parameters, tends to converge towards a steady hopping height. In this particular case, the equilibrium height approximates 165mm.

Experimental Parameters	Values
Hopper body rest length(m)	0.13
Body mass(kg)	2.362
Foot mass(kg)	0.497
Ground stiffness(N/m)	$> 10^9$
Leg stiffness(N/m)	2319
Ground damping(N*s/m)	0
Leg damping(N/m)	2.83
Pre-compression(mm)	2.5

Table 5.2: Parameters of equilibrium height experiment.

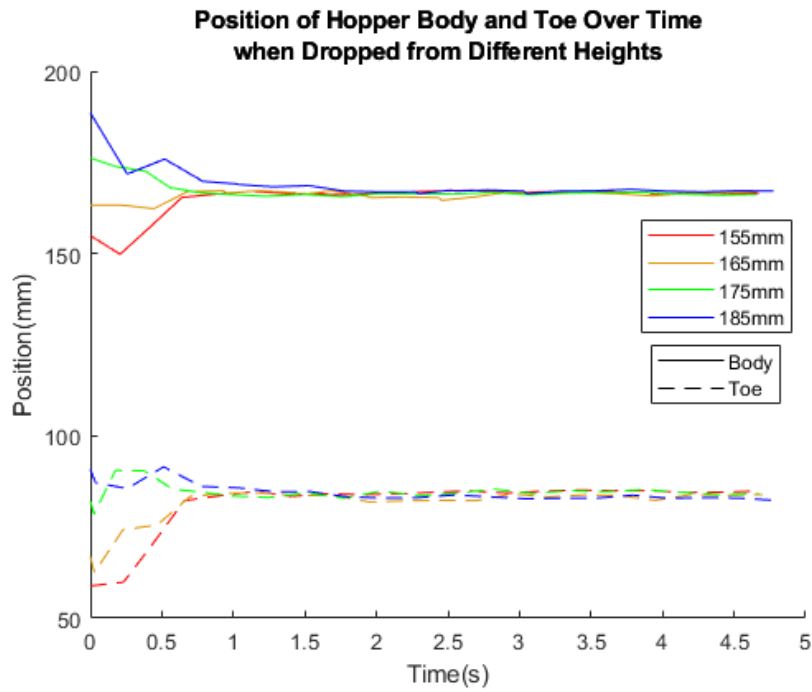


Figure 5-3: Trajectory of hopper body and foot in equilibrium height experiment.

### 5.3 1D Hopping Energy Consumption

This section presents the simulation findings that demonstrate the optimization of energy expenditure through the use of a leg with tunable stiffness while maintaining identical hopping heights across different ground stiffnesses. The parameters utilized in the simulation are outlined in Table 5.3. The previous model computes the tendon compression necessary to attain the Equilibrium (EQL) height, which is a relative height above the initial body height.

Two distinct data sets were simulated. Figure 5-4a presents a scenario where the damping coefficients of the ground and leg are 10 and 5, respectively. Conversely, Figure 5-4b illustrates a different situation, where the damping coefficients of the ground and leg are 2 and 5, respectively. The two figures present contrasting outcomes. They suggest that when the leg is less damped than the ground, a softer leg on softer ground dissipates less energy compared to a harder leg. In contrast, a harder leg consumes less energy compared to a softer leg on harder ground. However, when the ground damping coefficient is smaller than that of the leg, a harder leg consistently proves to be more energy-efficient.

Simulation Parameters	Values
Relative hopping height(m)	0.02
Body mass(kg)	1.5
Foot mass(kg)	0.25
Ground stiffness(N/m)	2000, 5000, 10000
Leg stiffness(N/m)	2000 to 10000

Table 5.3: Parameters of damping energy loss simulation.

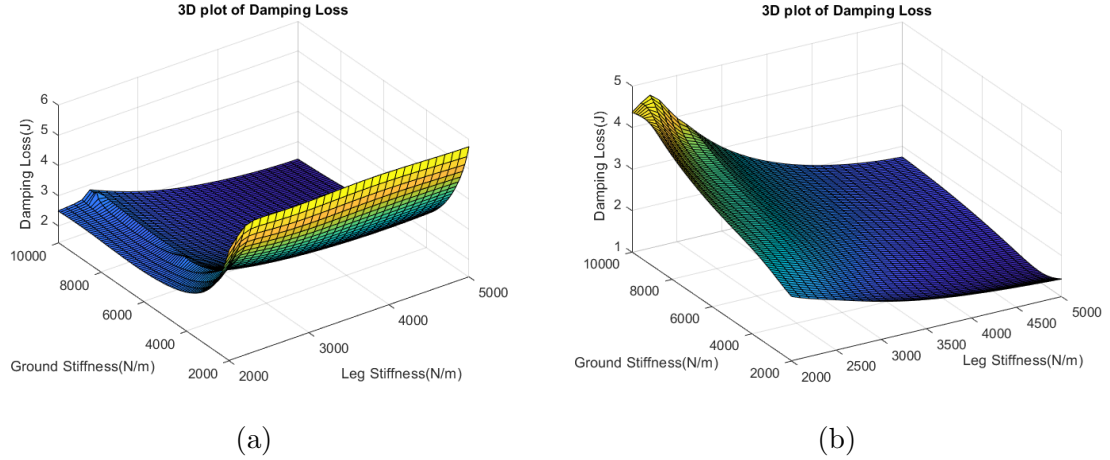


Figure 5-4: Results of the damping energy loss simulation. (a) Damping loss when ground damping coefficient  $d_g = 10$ , leg damping coefficient  $d_l = 5$ . (b) Damping loss when ground damping coefficient  $d_g = 2$ , leg damping coefficient  $d_l = 5$ .

In an effort to validate our initial findings, a series of experiments were conducted wherein the real-time power output of the U8 motor was monitored to estimate the total energy expenditure. To mitigate any influence of gravitational energy on the results, the hopper was set to release at a height of 40mm above the ground, and it was observed (by Tracker) to maintain an equilibrium height of 20mm after several hops. The pre-compression length was adjusted to ensure this balance was achieved when the hopper leg altered its stiffness or the ground material was switched.

Data collection commenced when the Inertial Measurement Unit (IMU) sensor detected free-falling, and it terminated when the number of impacts met the pre-set limit. As illustrated in Figure 5-5a, the initial phase of hopping (0-0.6s) showed some instability, with significant torque and power output spikes that could potentially skew the results. To circumvent this, data was collected only after three hops, recording both the energy expenditure and total time. This modified approach yielded a more consistent waveform, as depicted in Figure 5-5b.

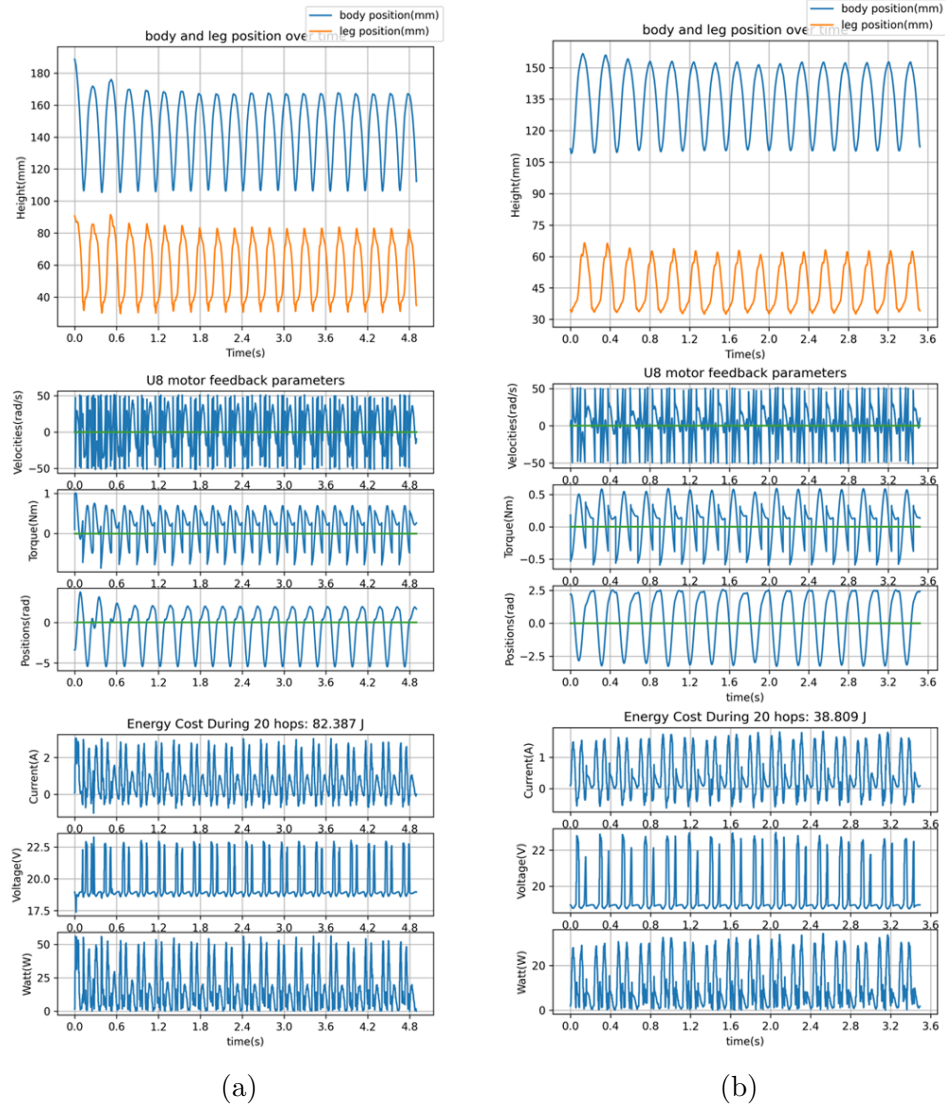


Figure 5-5: (a) Example data with unstable hops at the beginning. (b) Example data after the hopper approach the equilibrium state.

The collected experimental data is detailed in Table 5.4. Only two leg stiffnesses were tested, with a 'soft' leg indicating zero air chamber compression and leg stiffness of 2319 N/m, while a 'hard' leg refers to the air chamber at its maximum compression with a leg stiffness of 3295 N/m. The specific materials utilized can be referenced in Table 4.1.

Table 5.4: Hopper ground test data

Leg stiffness	Ground stiffness	Pre-compression (mm)	Energy consumption(J)	Hopping time (s)	Average energy per second (Watt)	Standard Deviation (Watt)
Soft	Hard	34	40.165	3.518	11.376	0.267
			40.746	3.499		
			38.809	3.492		
Soft	Medium	37	44.471	3.679	12.747	0.607
			46.653	3.512		
			45.970	3.572		
Soft	Soft	56	74.779	4.153	17.647	0.366
			68.753	3.980		
			70.548	3.995		
Hard	Hard	29	29.162	3.672	8.040	0.197
			27.723	3.504		
			27.735	3.355		
Hard	Medium	33	33.638	3.832	9.026	0.268
			33.720	3.622		
			32.909	3.661		
Hard	Soft	53	68.419	4.097	16.364	0.293
			66.701	4.108		
			65.064	4.027		

The results from the experiment demonstrate that a harder leg is more energy-efficient on both hard and soft ground, which aligns with the simulation trend shown in Figure 5-4b. A quantitative analysis reveals a remarkable enhancement in the

energy efficiency of the hopper with increased leg stiffness. Specifically, there is a substantial reduction in energy expenditure by 29.3% on hard ground and 29.2% on medium stiffness ground. Meanwhile, on soft ground, the energy savings are found to be 7.3%. These outcomes substantiate the significance of leg stiffness in optimizing the hopper's energy utilization across different terrains. Specifically, when the leg exhibits more damping than the ground, a stiffer leg dissipates less energy compared to a softer leg.

However, due to the limitations of the current experimental apparatus, there is an ongoing search for more significantly damped materials possessing a larger damping coefficient than the pneumatic bellow leg. Future work will involve conducting further experiments to ascertain whether the proposed efficient locomotion strategy can be empirically confirmed.

# Chapter 6

## Conclusion

### 6.1 Summary

The principal objective of this thesis was to design, model, and test a hopping robot equipped with a tunable-stiffness leg. In pursuit of this goal, we constructed models for the pneumatic bellows actuator, the hopper leg, and the hopping dynamics. This work also entailed designing the mechanical structure for the hopper, in addition to developing the necessary hardware and software systems for sensing and controlling the actuation. In order to validate our theoretical understanding, a set of experiments were meticulously planned and executed. The results elucidated the relationship between the energy expenditure in hopping and leg stiffness, demonstrating an alignment with our simulation findings. The result supports that within a land that is less damped than the leg, a harder leg will always be more energy efficient.

### 6.2 Future Work

The current work presents multiple prospects for further exploration and refinement. A key focus is to investigate the relationship between energy efficiency and leg stiffness under varying ground conditions. Our simulations suggest the need for experiments

on the ground with greater damping properties, potentially in the form of granular materials. Alternatively, constructing a ground emulator, powered by a motor to simulate ground movement during hopping, might serve as a promising solution.

Moreover, several aspects of the current system can be improved, such as enhancing airtightness, expanding the stiffness range, and refining the motor controller. Given the verification of the energy efficiency theory, we plan to integrate additional sensors on the hopper to actively monitor ground conditions. Control of the hopping robot will also be an interesting topic, promoting the development of a more advanced controller for this monopodal robot system.

### **6.3 Lessons Learned**

Finishing my Master's thesis is like wrapping up a two-year-long adventure, but it's just the start of my bigger journey in the world of research. Over the last year, I've been deep into research and really understood what it's all about. In essence, I have come to perceive research as a continual cycle of identifying problems and crafting solutions. This journey has been dealing with challenges from diverse fields, including mathematics, mechanics, electronics, and software, each of which I am proud to have overcome.

One of the most invaluable lessons I have gained from this experience is problem-solving and critical thinking. I have become proficient in the art of dissecting complex issues, learning to systematically delve into background knowledge, propose potential solutions, and validate these hypotheses.

Furthermore, I have learned the significance of collaboration and teamwork in research. Being a team leader teaches me the responsibility of leading by example and the task of leveraging each member's unique capabilities to attain our collective goals.

Finally, the passion for exploration, creation, and truth-seeking, is the fuel that drives research. It forms the bedrock of any successful research endeavor.

Now, as I stand at the threshold of a new chapter in my academic journey, I am excited and prepared to use the knowledge and skills I have acquired to achieve the next milestone!

# References

- [1] Sangbae Kim, Patrick M Wensing, et al. Design of dynamic legged robots. *Foundations and Trends® in Robotics*, 5(2):117–190, 2017.
- [2] Rhodri Armour, Keith Paskins, Adrian Bowyer, Julian Vincent, and William Megill. Jumping robots: a biomimetic solution to locomotion across rough terrain. *Bioinspiration & biomimetics*, 2(3):S65, 2007.
- [3] Wei-Hsi Chen, Shivangi Misra, J Diego Caporale, Daniel E Koditschek, Shu Yang, and Cynthia R Sung. A tendon-driven origami hopper triggered by proprioceptive contact detection. In *2020 3rd IEEE International Conference on Soft Robotics (RoboSoft)*, pages 373–380. IEEE, 2020.
- [4] Chi Zhang, Wei Zou, Liping Ma, and Zhiqing Wang. Biologically inspired jumping robots: A comprehensive review. *Robotics and Autonomous Systems*, 124:103362, 2020. ISSN 0921-8890. doi: <https://doi.org/10.1016/j.robot.2019.103362>. URL <https://www.sciencedirect.com/science/article/pii/S0921889019301861>.
- [5] Marshall H Kaplan and Howard S Seifert. Hopping transporters for lunar exploration. *Journal of Spacecraft and Rockets*, 6(8):917–922, 1969.
- [6] Aji Sayyad, B Seth, and P Seshu. Single-legged hopping robotics research—a review. *Robotica*, 25(5):587–613, 2007.

- [7] Elliot W Hawkes, Charles Xiao, Richard-Alexandre Peloquin, Christopher Keeley, Matthew R Begley, Morgan T Pope, and Günter Niemeyer. Engineered jumpers overcome biological limits via work multiplication. *Nature*, 604(7907): 657–661, 2022.
- [8] Duncan W Haldane, Justin K Yim, and Ronald S Fearing. Repetitive extreme-acceleration (14-g) spatial jumping with salto-1p. In *2017 IEEE/RSJ International Conference on Intelligent Robots and Systems (IROS)*, pages 3345–3351. IEEE, 2017.
- [9] Valentin Zaitsev, Omer Gvirsman, Uri Ben Hanan, Avi Weiss, Amir Ayali, and Gabor Kosa. A locust-inspired miniature jumping robot. *Bioinspiration & biomimetics*, 10(6):066012, 2015.
- [10] Ryuma Niiyama, Akihiko Nagakubo, and Yasuo Kuniyoshi. Mowgli: A bipedal jumping and landing robot with an artificial musculoskeletal system. In *Proceedings 2007 IEEE International Conference on Robotics and Automation*, pages 2546–2551. IEEE, 2007.
- [11] Matthew F. Hale, Jonathan L. Du Bois, and Pejman Iravani. Agile and adaptive hopping height control for a pneumatic robot. In *2018 IEEE International Conference on Robotics and Automation (ICRA)*, pages 5755–5760, 2018. doi: 10.1109/ICRA.2018.8460557.
- [12] Minkyun Noh, Seung-Won Kim, Sungmin An, Je-Sung Koh, and Kyu-Jin Cho. Flea-inspired catapult mechanism for miniature jumping robots. *IEEE transactions on robotics*, 28(5):1007–1018, 2012.
- [13] Mihai Duduta, Florian Berlinger, Radhika Nagpal, David R Clarke, Robert J Wood, and F Zeynep Temel. Tunable multi-modal locomotion in soft dielectric elastomer robots. *IEEE Robotics and Automation Letters*, 5(3):3868–3875, 2020.

- [14] Sangbae Kim, Cecilia Laschi, and Barry Trimmer. Soft robotics: a bioinspired evolution in robotics. *Trends in biotechnology*, 31(5):287–294, 2013.
- [15] Loïc Blanc, Alain Delchambre, and Pierre Lambert. Flexible medical devices: Review of controllable stiffness solutions. In *Actuators*, volume 6, page 23. MDPI, 2017.
- [16] Stephen Coyle, Carmel Majidi, Philip LeDuc, and K Jimmy Hsia. Bio-inspired soft robotics: Material selection, actuation, and design. *Extreme Mechanics Letters*, 22:51–59, 2018.
- [17] Mariangela Manti, Vito Cacucciolo, and Matteo Cianchetti. Stiffening in soft robotics: A review of the state of the art. *IEEE Robotics & Automation Magazine*, 23(3):93–106, 2016.
- [18] Jun Zhang, Jun Sheng, Ciarán T O’Neill, Conor J Walsh, Robert J Wood, Jee-Hwan Ryu, Jaydev P Desai, and Michael C Yip. Robotic artificial muscles: Current progress and future perspectives. *IEEE transactions on robotics*, 35(3): 761–781, 2019.
- [19] Sonia F Roberts and Daniel E Koditschek. Virtual energy management for physical energy savings in a legged robot hopping on granular media. *Frontiers in Robotics and AI*, 8:740927, 2021.
- [20] Hung Q Vu and Lorenzo G Marcantini. Knee stiffness adjustment for energy efficient locomotion of a legged robot on surfaces with different stiffness. In *2013 IEEE International Conference on Robotics and Biomimetics (ROBIO)*, pages 1825–1831. IEEE, 2013.
- [21] Hung Q Vu, Helmut Hauser, Derek Leach, and Rolf Pfeifer. A variable stiffness mechanism for improving energy efficiency of a planar single-legged hopping robot. In *2013 16th International Conference on Advanced Robotics (ICAR)*, pages 1–7. IEEE, 2013.

- [22] Kevin C Galloway, Jonathan E Clark, Mark Yim, and Daniel E Koditschek. Experimental investigations into the role of passive variable compliant legs for dynamic robotic locomotion. In *2011 IEEE International Conference on Robotics and Automation*, pages 1243–1249. IEEE, 2011.
- [23] Ali Shiva, Agostino Stilli, Yohan Noh, Angela Faragasso, Iris De Falco, Giada Gerboni, Matteo Cianchetti, Arianna Menciassi, Kaspar Althoefer, and Helge A Wurdemann. Tendon-based stiffening for a pneumatically actuated soft manipulator. *IEEE Robotics and Automation Letters*, 1(2):632–637, 2016.
- [24] Nadia G Cheng, Maxim B Lobovsky, Steven J Keating, Adam M Setapen, Katy I Gero, Anette E Hosoi, and Karl D Iagnemma. Design and analysis of a robust, low-cost, highly articulated manipulator enabled by jamming of granular media. In *2012 IEEE international conference on robotics and automation*, pages 4328–4333. IEEE, 2012.
- [25] Hugo Rodrigue, Wei Wang, Min-Woo Han, Thomas JY Kim, and Sung-Hoon Ahn. An overview of shape memory alloy-coupled actuators and robots. *Soft robotics*, 4(1):3–15, 2017.
- [26] Wanliang Shan, Tong Lu, and Carmel Majidi. Soft-matter composites with electrically tunable elastic rigidity. *Smart Materials and Structures*, 22(8):085005, 2013.
- [27] Alì Sadeghi, Lucia Beccai, and Barbara Mazzolai. Innovative soft robots based on electro-rheological fluids. In *2012 IEEE/RSJ international conference on intelligent robots and systems*, pages 4237–4242. Ieee, 2012.
- [28] Vincent Wall, Raphael Deimel, and Oliver Brock. Selective stiffening of soft actuators based on jamming. In *2015 IEEE International Conference on Robotics and Automation (ICRA)*, pages 252–257. IEEE, 2015.

- [29] Wei-Hsi Chen, Shivangi Misra, Yuchong Gao, Young-Joo Lee, Daniel E Koditschek, Shu Yang, and Cynthia R Sung. A programmably compliant origami mechanism for dynamically dexterous robots. *IEEE Robotics and Automation Letters*, 5(2):2131–2137, 2020.
- [30] Wyatt Felt, Matthew A Robertson, and Jamie Paik. Modeling vacuum bellows soft pneumatic actuators with optimal mechanical performance. In *2018 IEEE International Conference on Soft Robotics (RoboSoft)*, pages 534–540. IEEE, 2018.
- [31] Dylan Drotman, Michael Ishida, Saurabh Jadhav, and Michael T Tolley. Application-driven design of soft, 3-d printed, pneumatic actuators with bellows. *IEEE/ASME Transactions on Mechatronics*, 24(1):78–87, 2018.
- [32] Shivangi Misra and Cynthia Sung. Forward kinematics and control of a segmented tunable-stiffness 3-d continuum manipulator. In *2022 International Conference on Robotics and Automation (ICRA)*, pages 3238–3244. IEEE, 2022.